Universidad Técnica Federico Santa María
Departamento de Ingeniería Eléctrica

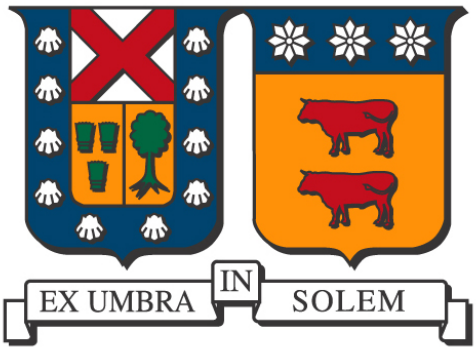

Model Predictive Current Control Based On Optimal Switching Sequences For Four-Leg Two-Level Active Power Filters

Thesis to qualify for the degree of Master of Science in Electrical Engineering

Author:
Felipe Ignacio Leiva Silva

Thesis advisor:
Dr. Andrés Mora Castro

October 18, 2023

Abstract

This work presents a versatile and effective model predictive current control strategy based on optimal switching sequences for four–leg two–level grid–connected converters, proving the potential of this type of converter and the proposed controller for shunt active filter applications. The controller presents an excellent dynamic performance, tracking of high-frequency reference signals, fixed switching frequency, and well-formed harmonic spectrum, enabling the proposed controller to govern active filters and distributed generation applications based on four–leg converters. Simulations and experimental results demonstrate the effectiveness and high-quality performance obtained with the proposed strategy.

In addition, a novel improvement is proposed to obtain the optimal result of the optimization problem based on the Active-Set Method. Simulations were performed to compare the results obtained with this improvement with another method, known as Unit Partition, and with a MATLAB solver probing that the result is optimal.

The performance of the proposed controller for shunt-active filter applications is verified through simulations to finally test its performance in a laboratory setup using an IGBT-based converter with an unbalanced and non-linear load.

Keywords: Three–phase four-wire converters, Active Filters, Distribution Systems, Model Predictive Control.

Resumen

Este trabajo presenta una estrategia de control de corriente predictivo versátil y eficaz basada en secuencias de conmutación óptimas para convertidores conectados a la red de dos niveles y cuatro piernas, demostrando el potencial de este tipo de convertidor y el controlador propuesto para ser utilizado en aplicaciones de filtro activo de corriente. El controlador presenta un excelente desempeño dinámico, seguimiento de señales de referencia de alta frecuencia, frecuencia de conmutación fija y espectro armónico adecuado, lo que permite que el controlador propuesto sobresalte en la aplicación de filtros activos y aplicaciones de generación distribuida basadas en convertidores de cuatro piernas. Las simulaciones y los resultados experimentales demuestran la efectividad y el desempeño de alta calidad obtenidos con la estrategia propuesta.

Por otro lado, se propone una mejora para el algoritmo propuesto de manera de poder obtener el resultado óptimo del problema de optimización. Se demostró el desempeño de esta mejora a través de simulaciones comparando los resultados obtenidos con otro método, conocido como Partición por Unidad, y con un solver de MATLAB, comprobando que el resultado obtenido es realmente óptimo.

Luego, a través de simulaciones, se prueba el desempeño del controlador propuesto en este trabajo para aplicaciones de filtro activo en derivación para finalmente comprobar su desempeño en pruebas de laboratorio utilizando un convertidor basado en IGBT y una carga desbalanceada y no lineal.

Palabras clave: Three-phase four-wire converters, Active Filters, Distribution Systems, Model Predictive Control.

Nomenclature

$3P3W$ Three-Phase Three-Wire

$3P4W$ Three-Phase Four-Wire

$4L-2L$ Four-Leg Two-Level

AC Alternate Current

APF Active Power Filter

ASM Active-Set Method

CCS Continuous Control Set

DC Direct Current

DG Distributed Generation

DN Distributed Networks

FCS Finite Control Set

MG Micro Grid

MPC Model Predictive Control

OSS Optimal Switching Sequence

OSV Optimal Switching Vector

PI Proportional Integral

PR Proportional Resonant

RE Renewable Energy

$REGS$ Renewable Energy Generation Systems

$UASV$ Unconstrained Average Switching Vector

VSC Voltage Source Converter

Contents

Nomenclature **4**

List of figures **7**

List of tables **9**

1 Introduction **10**
1.1 Hypothesis . . . 12
1.2 Objectives . . . 12
1.2.1 Main Objective . . . 12
1.2.2 Specific Objectives . . . 12
1.3 Work Methodology . . . 13

2 State of art of Model Predictive Control **14**
2.1 Basic principles of MPC . . . 15
2.2 Continuous Control Set MPC . . . 16
2.3 Finite Control Set MPC . . . 17
2.3.1 Optimal Switching Vector MPC . . . 17
2.3.2 Optimal Switching Sequence MPC . . . 18

3 Theoretical background **19**
3.1 Grid-Connected Power Converters . . . 19
3.2 Current Controllers for Active Filter Applications . . . 21
3.2.1 Proportional Integral controllers . . . 22
3.2.2 Hysteresis controllers . . . 22
3.2.3 Poportional Resonant controller . . . 22
3.2.4 Finite Control Set MPC . . . 23
3.3 Current Harmonic Requirements . . . 24
3.4 Description of the 4L-2L VSC . . . 25

4 Proposed Optimal Switching Sequence MPC Strategy **29**
4.1 OSS-MPC for 4-Leg Grid-Tied Converters . . . 29

4.1.1 Continuous-Time Model 29
4.1.2 Discrete-Time Model: The Average Trajectory 30
4.1.3 Optimal Control Problem 32
4.1.4 Duty Cycles Calculation 33
4.1.5 Cost function minimization and OSS selection 35
4.1.6 Tuning of the controller 36
4.1.7 OSS Implementation 37
4.1.8 Kalman filter 37
4.1.9 Computation of future references and grid voltage 38
4.1.10 Summary of the proposed method 39

5 Simulation and Experimental results **41**
5.1 Simulation results 41
5.2 Experimental results 44
5.2.1 Steady-State Performance 45
5.2.2 Effect of the Tuning Parameters. 48
5.2.3 Dynamic Performance. 50
5.2.4 Execution time of the proposed control strategy 50
5.2.5 Assessment as a Shunt Active Filter 51
5.2.6 Impact of the Parameters Mismatch 52

6 Conclusions **56**

Appendix **57**

A Table of tetrahedra and Switching Sequence **58**

B Images of Laboratory Setup **62**

Bibliography **64**

List of Figures

1.1 Representation of a typical electrical system 11

2.1 Classification of MPC strategies applied to power converters and drives. Figure taken from [1] 15
2.2 Grid-connected 4L-2L VSC. 15
2.3 General scheme of basic MPC. 16

3.1 Basic interface of shunt active filter. 20
3.2 An hysteresis current control for a three-phase two-level power converter: (A)operation principle and (B) block diagram. 23
3.3 Grid-connected 4L-2L VSC. 25
3.5 (a) Top view of the control region of the 4L-2L-VSI over the $\alpha\beta$ -plane. (b) The four tetrahedra that form the extension of sector $\mathcal{S}_2$ over γ axis (tetrahedron $\mathcal{T}_5$ to $\mathcal{T}_8$) 26
3.4 Control region in the $\alpha\beta\gamma$ space for the 4L-2L-VSI. $\alpha\beta\gamma$ are in pu . . . 27

4.1 Grid-connected 4L-2L VSC. 30
4.2 Symmetrical 9S-SS for the tetrahedron $\mathcal{T}_7(4, 12, 13)$. 31
4.3 Predicted system trajectory for a 9S-SS. 31
4.4 Subregions of the outer face of every tetrahedron 35
4.5 Single-carrier-based PWM to synthesize the desired SS. 36
4.6 Flowchart of the proposed current control strategy. 40

5.1 (a) Positive- and zero-sequence current step-changes, both at the fundamental frequency, (b) Zero-sequence current step-change of 250 Hz (c) sinusoidal and triangular references, respectively. 42
5.2 Transient response of the proposed MPC strategy. u_{op} is the optimal solution obtained with Matlab solver and u_{uc} corresponds to the solution obtained with proposed scheme showed in section 4.1.4. (a) u_{uc} response to step-change in $\alpha\beta$ current-references (b) Zoom of image in (a). 43
5.3 Comparison of the proposed MPC strategy and PR controller. (a) Step-change in $\alpha\beta$ currents and (b) Step-change in γ current. 44

5.4 Comparison of the proposed MPC strategy and PR controller. (a) Step-change in $\alpha\beta$ grid-voltages and (b) Step-change in γ grid-voltage. 44
5.5 Laboratory setup diagram. 45
5.6 Steady-state performance at f_s=5 kHz: (a) PF=1; (b) PF = 0. 45
5.7 Steady-state performance at f_s=7.5 kHz: (a) PF =1; (b) PF = 0. . . . 46
5.8 Experimental current TDD at rated power as function of the power factor for three switching frequencies. 46
5.9 Effect of the tuning parameter $\lambda_u^{\alpha\beta}$ on the transient performance while keeping λ_u^{γ} constant: sinusoidal references. 47
5.10 Effect of the tuning parameter $\lambda_u^{\alpha\beta}$ on the transient performance while keeping λ_u^{γ} constant: triangular reference for current i_g^{γ}. 47
5.11 Effect of the tuning parameter λ_u^{γ} on the transient performance while keeping $\lambda_u^{\alpha\beta}$ constant: sinusoidal references. 48
5.12 Effect of the tuning parameter λ_u^{γ} on the transient performance while keeping $\lambda_u^{\alpha\beta}$ constant: triangular reference for current i_g^{γ}. 49
5.13 (a) Positive- and zero-sequence current step-changes, both at the fundamental frequency and (b) Zero-sequence current step-change of 250 Hz. 49
5.14 Execution time of the proposed control strategy. 50
5.15 Computational. 51
5.16 Reference generator used in this work to obtain the current reference for the controller. LPF = Low Pass Filter and PLL = Phase-Locked Loop. Current references are: $i_d^{\star} = -\tilde{i}_d$ and $i_q^{\star} = -\left(\bar{i}_q + \tilde{i}_q\right)$, where the variables $\tilde{i}$ and $\bar{i}$ are the sinusoidal and average component of the current. 51
5.17 Unilineal diagram of the experimental setup used for testing the shunt active filter. 52
5.18 Shunt active filter operation at f_s=5 kHz: (a) source voltage v_{sa} and current i_{sa}; (b) converter current i_{fa} (filter current); and (c) source neutral current i_{sn}. 53
5.19 FCS-MPC performance: (a) v_{sa} and i_{sa}; (b) i_{fa}; and (c) i_{sn}. 53
5.20 Effect of parameter mismatch on the controller system performance: (a) overestimated inductance $\mu_L = 1.5$; and (b) underestimated inductance $\mu_L = 0.5$. Switching frequency 5 kHz. 54
5.21 Effect of parameter mismatch on the controller system performance: (a) overestimated resistance $\mu_R = 1.5$; and (b) underestimated resistance $\mu_R = 0.5$. Switching frequency 5 kHz. 55

B.1 Laboratory setup used for empirical results. 63
B.2 Inside of the rack used to store the converter and control platform. . . 63

List of Tables

3.1 Table extracted from [2]. Harmonic content limit accepted by the standard for voltage systems between 120 [V] and 69 [kV] 25
3.2 Switching states of a 4L-2L converter. Voltage values normalized by V_{dc}. 26

5.1 Parameters of the Experimental Setup phase and neutral inductance have a value of 10% and 5% of the base impedance, respectively. 41

A.1 Tretrahedrons gruped by sectors. 59

Chapter 1

Introduction

The utility industries across the world are trying to address numerous challenges, including generation diversification, optimal deployment of expensive assets, demand response, energy conservation, and reduction of the industry overall carbon footprint. It is evident that such critical issues cannot be addressed within the confines of the existing electricity grid. The general structure of an electrical interconnected system is presented in Fig. 1.1. Electrical energy is generated in large-scale facilities that are located away from final users. Afterward, energy is transferred to the final customers through high-voltage transmission lines and distribution power systems. Therefore, this electrical system structure is known as centralized generation and it is unidirectional in nature. In this hierarchical configuration, a failure in any component is transferred to other components in the chain and may result in poor power quality, power cuts, or even blackouts. [3]

During the last few years, there has been a rapid evolution and a decrease in costs of renewable energy generation systems (REGS) such as photovoltaic energy, wind energy, and storage systems among others [4]. Therefore, instead of using large generation centers, there has been an increase in the appearance of generation units dispersed throughout the entire electrical network. In this way, the traditional scheme of power electric systems observed in Fig. 1.1, has slowly been displaced to what is known today as Distributed Generation (DG) [5, 6]. In this context, in addition to other factors such as the appearance of electromobility and government policies to promote the installation of renewable energy systems, power converters are essential for the incorporation of REGS systems into electric power systems. One positive characteristic of these interfaces is that they can be used not only for delivering energy from the renewable source to the grid, but also for creating a more flexible and efficient electrical system. Due to all the aforementioned, the new concept of Micro Grids (MG) has been introduced in literature [7]. But, due to the high presence of power electronic devices in this type of system, a high current harmonic content is produced. High levels of harmonic current can cause problems such as unnecessary losses and heat in power system transformers, nuisance tripping of circuit breakers,

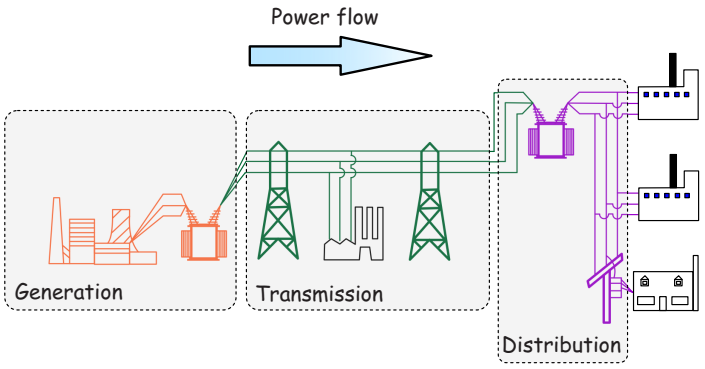

Figure 1.1: Representation of a typical electrical system

and over-stressing of power factor correction capacitors.

Harmonic distortion has traditionally been dealt with by the use of passive LC filters. However, the application of passive filters for harmonic reduction may result in parallel resonances with the network impedance, over-compensation of reactive power at fundamental frequency, and poor flexibility for dynamic compensation of different frequency harmonic components. Another solution to minimize current harmonic content are Active Power Filter (APF). The advantage of active filtering is that it automatically adapts to changes in the network and load fluctuations. They can compensate for several harmonic orders and are not affected by major changes in network characteristics, eliminating the risk of resonance between the filter and network impedance. Another plus is that they take up very little space compared with traditional passive compensators [4].

Low voltage MGs and Distributed Networks (DN) are typically unbalanced electric grids [8, 9], and their network structures are: (i) three-phase three-wire (3P3W) and (ii) three-phase four-wire (3P4W) systems. In low-voltage systems, a two-level converter is enough for active filter applications. The four-leg converter topology is a promising solution compared with the three-leg inverters with split DC-bus to solve the output power quality issues and achieve transformerless operation [10]. The output current control of this converter topology is a critical aspect in 3P4W applications such as DG units [11], shunt active filters [12–14], and sharing of unbalanced load in MG [15]. Accordingly, some of the desired features of the current control are (i) accurate current control; (ii) high bandwidth; (iii) fast dynamic response; and (iv) low harmonic distortion. Aiming to fulfill these features, many control strategies such as proportional-integral (PI) controllers in synchronous reference frames, proportional-resonant (PR) controllers, repetitive controllers (RC), deadbeat and model predictive controllers, among others, have been proposed in the literature [16].

In this work, a current controller based on MPC-OSS is proposed for a 4L-2L converter. Simulation and experimental results are obtained to show the potential of this controller and converter working as a shunt active filter. A DSP+FPGA platform was utilized to program the control strategy and modulate the signals sent

to the converter. Also, simulations for a PR controller were carried out to prove the superiority of the proposed controller. All this test were performed to finally accomplished laboratory results using a converter based on IGBT's semiconductors and an unbalanced-reactive non-linear load probing its well-performance compensating harmonic and zero-sequence currents.

1.1 Hypothesis

The controller is expected to meet the following characteristic:

- It can be implemented in low-cost control platforms without degrading the inherent fast dynamic response of FCS-MPC.
- It enables the converter to operate with a fixed switching frequency and a predefined harmonic spectrum.
- The control algorithm efficiently determines the optimal region and the application times of its switching vectors to provide the optimal switching sequence with a reduced computational burden.
- The controller is simple to design and tune, achieving good tracking of signals having high-content of harmonic components like triangular and trapezoidal waveforms.

Due to the high performance of the controller, it is expected that it is suitable to be used for shunt active filter applications.

1.2 Objectives

1.2.1 Main Objective

To design and implement a predictive control scheme with vector modulation for a 4L-2L converter for active current filter applications.

1.2.2 Specific Objectives

- Review the current literature of MPC, characterize how the four-leg converter works, and search the regulatory requirements in the electrical standards on the harmonic content in distribution networks.
- Propose a predictive control strategy for a four-leg converter connected to the network to enhance the harmonic distortion obtained with the proposed strategy.
- A novel improvement will be formulated to achieve optimal solution of the objective function during over-modulation cases.
- Validate the proposed strategy through simulations analyzing its performance and comparing it with the traditional resonant controller.

- Implement a laboratory setup to test the performance of the proposed control strategy with a 4L-2L converter connected as a shunt active filter with a non-linear unbalanced load.

1.3 Work Methodology

This thesis can be divided into five stages, where each one is strictly related to the objectives initially set.

The first two stages corresponds to the theoretical work (collection and modeling of the system), where the existing bibliography of the different predictive control strategies for three-leg converters should be reviewed and their operation and extrapolate it to a four-leg converter. For this, a bibliographical review of the switching states of the four-legged converters and their representation in the $\alpha\beta\gamma$ plane will be carried out, identifying the tetrahedrons that are generated and thus being able to mathematically formulate the appropriate predictive control scheme for this topology.

The third stage consist of running simulations using the softwares Matlab and Plecs that will be carried out to validate the results obtained within the next stage in the laboratory setup. Also, comparisons with traditional proportional-resonant controller will be carried out to demonstrate the merits of the proposed method. In this context, the response to reference changes and disturbances at the input of the system is compared.

The fourth stage of the work considers carrying out an experimental work, which will consist of starting up the four-leg converter connected to the network with an inductive filter between the grid and the converter, using the control strategy developed in the first and second stages. Finally, stationary state and dynamic tests will be performed to show up the good performance of the proposed strategy at different switching frequencies and in current references of different frequencies, demonstrating the benefits of using this kind of converter with this strategy as an active filter of harmonic and zero-sequence currents.

The final stage consists of adding an unbalanced and non-linear load to the setup constructed in the previous stage with the aim of presenting the performance of the proposed current controller. A reference generator will be implemented to calculate the current references that the controller needs to compensate for reactive power, harmonic and zero-sequence currents.

Chapter 2

State of art of Model Predictive Control

The main characteristic of predictive control is the use of a model of the system for predicting the future behavior of the controlled variables. This information is used by the controller to obtain the optimal actuation, according to a predefined optimization criterion. This structure has several important advantages [17]:

- Concepts are very intuitive and easy to understand.
- The multivariable case (MIMO) can be easily considered.
- Easy inclusion of non linearities in the model.
- Simple treatment of constraints and suitable for inclusion of modifications.
- Directly defines the switching sequence S_w, without needing anything else.

Nevertheless, MPC presents some disadvantages:

- High computational cost.
- The quality of the model has a direct influence on the quality of the controller, i.e., is highly sensitive to parameters estimation.
- If the system parameters change over time, estimation algorithms that consider these changes must be adapted or generated.

The MPC methods are classified according to the type of the optimization problem formulation [18]. Fig.2.1 shows the two principal classifications for MPC. On one hand, continuous control set MPC (CCS-MPC) computes a continuous control signal and then uses a modulator to synthesize the desired output voltage in the power converter. The main advantage of CCS-MPC is that it produces a fixed switching frequency due to the modulation stage. On the other hand, finite control set MPC (FCS-MPC) takes into account the discrete nature of the power converter to formulate the MPC algorithm and does not require an external modulator.

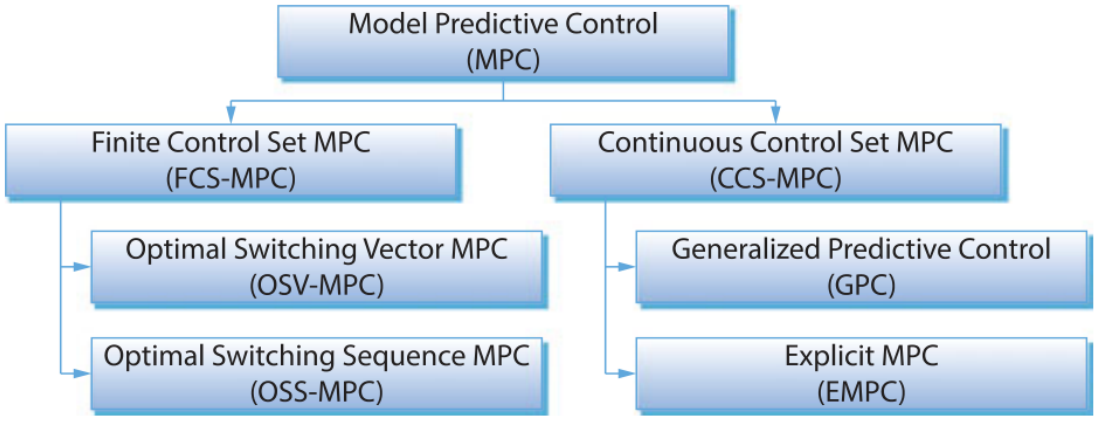

Figure 2.1: Classification of MPC strategies applied to power converters and drives. Figure taken from [1]

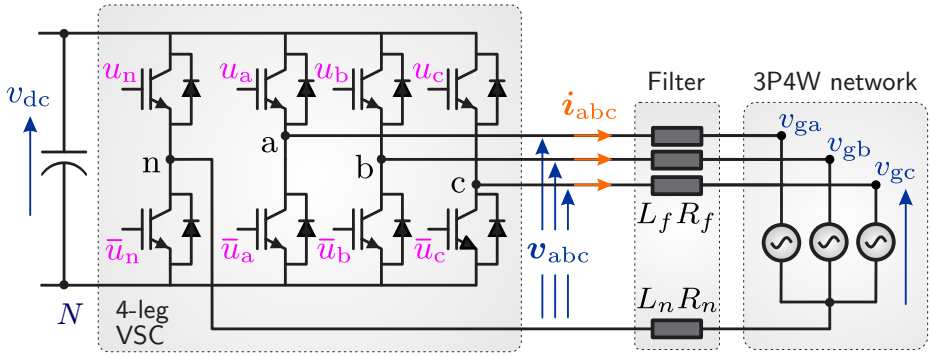

Figure 2.2: Grid-connected 4L-2L VSC.

2.1 Basic principles of MPC

MPC is a class of controllers that explicitly uses the model of the system to be controlled [1]. In general, MPC defines the control action by minimizing a cost function that describes the desired system behavior. This cost function weights the predicted system output with a reference where the predicted outputs are computed from the system model. For example, if the control variable is the current of the system then the cost function could be defined as the quadratic error of the current: $J = ||\boldsymbol{i}_s^\star(k) - \boldsymbol{i}_s(k+1)||^2$ where the current $\boldsymbol{i}_s(k+1)$ is obtained by using the model system.

To illustrate the use of MPC for power electronics, a basic MPC strategy with a prediction horizon equal to one, applied to the current control of a voltage source inverter (VSI) with RL load, is shown. The basic block diagram of this control strategy is presented in Fig. 2.3, where the reference and predicted currents at instant k + 2 are used in order to compensate for the digital implementation delay [19].

The algorithm is repeated for every switching period performing the following

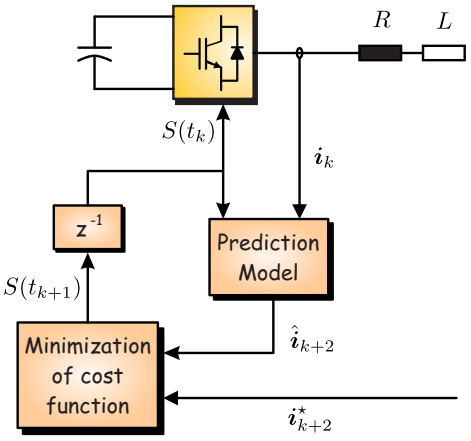

Figure 2.3: General scheme of basic MPC.

steps:

1. Optimal control action ($S(t_k)$) computed at instant t_{k-1} is applied to the converter.
2. Current $\boldsymbol{i}_k$ is measured at instant k. Also, the current reference $\boldsymbol{i}^{\star}_{k+2}$ is computed for instant $k+2$.
3. The predicted current $\hat{\boldsymbol{i}}_{k+2}$ is obtained through the system model.
4. Cost function is evaluated using $\boldsymbol{i}^{\star}_{k+2}$ and $\hat{\boldsymbol{i}}_{k+2}$. The optimal solution is determined by choosing the optimal control action ($S(t_k)$) that minimizes the function cost.

2.2 Continuous Control Set MPC

When a modulation stage is added to the control scheme the outputs of the controller are the duty cycles $d_i \in [0, 1]$. Thus, the decision variables of the optimization problem are continuous, typically resulting in a quadratic program (QP) [17].

CCS-MPC normally uses the discrete state-space model of the system defined as:

$$\boldsymbol{x}(k+1) = A\boldsymbol{x}(k) + B\boldsymbol{u}(k) \tag{2.1}$$

with $\boldsymbol{u}(k) \in \Re^n$. Also, the cost function is usually defined as the error tracking of the state variables:

$$J(k) = ||\boldsymbol{x}^{\star}(k) - \boldsymbol{x}(k+1)||^2 \tag{2.2}$$

Due to the modulation stage there is no need to add a second term to penalize the control effort, but it could be added to limit the transient response of the system. Therefore, this control method computes the voltage reference by minimizing the given cost function, representing the tracking error of the controlled variables. If no

constraints are considered, the optimal calculation vector can be easily obtained by solving $\nabla J = 0$. Otherwise, if constraints are considered for the MPC formulation, then more complex solvers must be employed to solve the optimal problem. The main disadvantage of this method is that the performance of the controller would be deteriorated by the parameter variations and non-linearity [20].

This category of MPC is normally divided into to groups: Generalized Predictive Control (GPC) and Explicit MPC (EMPC). Some claim that GPC corresponds to the first type of MPC control. It is also characterized to be useful for linear and unconstrained problems. Moreover, EMPC is suitable for non-linear and constrained systems [1]. CCS-MPC usually has a lower computational cost compared to FCS-MPC because it computes part of all the optimization problem off-line. GPC uses an expression to obtain the control action that can be calculated beforehand [21]. Alternatively, EMPC computes the optimal problem solution off-line, so the on-line calculations are limited to a search algorithm [22].

2.3 Finite Control Set MPC

The main difference of FCS-MPC in contrast with the CCS-MPC is that the optimal solution lies within a limited set of options. In consequence, the optimal problem is transformed into an enumerated search algorithm where the prediction variables and the cost function (J) are evaluated for all feasible inputs of the system. When using a power converter that has finite amount of switching states the cost function needs to be evaluated only for these limited cases. The prediction model is defined just like in (2.1) but in this case the input of the system is $\boldsymbol{u}(k) \in \{\boldsymbol{u}_1, \boldsymbol{u}_2, ..., \boldsymbol{u}_n\}$ where n is an integer value and it is equal to the total number of switching states of the power converter. Furthermore, equation (2.3) shows the cost function usually defined for FCS-MPC. The second term has been added to penalize the switching effort and λ_u is a weighting factor design to adjust the importance of this term.

$$J = ||\boldsymbol{x}^{\star}(k) - \boldsymbol{x}(k+1)||^2 + \lambda_u |\Delta u(k)| \tag{2.3}$$

This class of MPC can be divided in the two following groups [1]:

2.3.1 Optimal Switching Vector MPC

The Optimal Switching Vector MPC (OSV-MPC) only synthesizes one voltage vector in a complete switching period (Fig. 2.4a presents a diagram of this method). Consequently, no modulation stage is required. However, this method could lead to apply the same voltage vector in several consecutive switching cycles, causing a variable switching frequency in the system, producing a dispersed harmonic spectrum and higher ripple in the waveforms synthesize by the converter. Therefore, the use of this method of FCS-MPC is not recommended for grid connected power converter applications, due to the harmonic constraints imposed by the grid codes [2]. Moreover, OSV-MPC controller produces a nonzero average steady-state tracking error [23, 24].

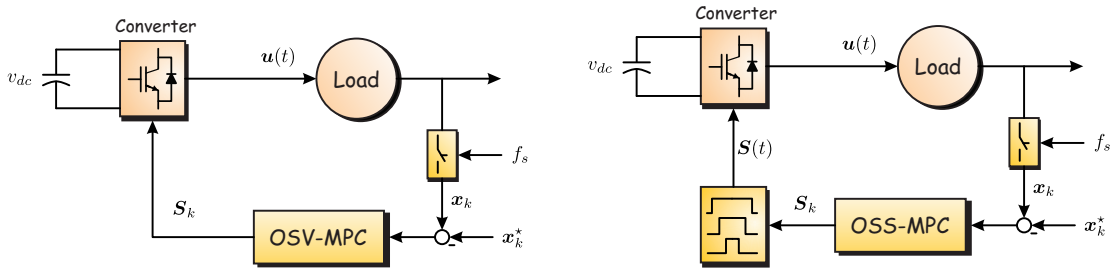

(a) OSV scheme. **(b)** OSS scheme

This disadvantage becomes relevant when the variable to be controlled is the active power to be injected into the grid [25, 26].

2.3.2 Optimal Switching Sequence MPC

Optimal Switching Sequence MPC (OSS-MPC) solves the harmonic spectrum problem caused in OSV-MPC considering a switching sequence instead of only one vector voltage in a switching period (Fig. 2.4b presents a diagram of this method). Because of this new consideration the OSS-MPC takes more computational burden since it adds the time application of the voltage vectors into the optimization problem. Thus, the optimal control problem considers the instants where one switching vector changes from one state to another, which is essentially what a modulator does. In consequence, a suitable modulation scheme is typically integrated into the OSS-MPC strategy to emulate the desired switching sequence easily.

Chapter 3

Theoretical background

3.1 Grid-Connected Power Converters

Power converters play an important role in DG and RE generation. They are also widely used in industrial applications such as energy storage systems, active-front-end rectifiers and power conditioning units [27].

Power converters are autonomous equipment, and therefore their performance does not only depend on the equipment design (topology) but also on the control strategy used. The following list enumerates the main operating requirements of a drive, not only related to the closed-loop response but also to the safe operation of the drive and the load (or network):

- Fixed or limited switching frequency: the importance of this characteristic is reflected in two points. On one hand, the switching frequency is related to the losses of the converter, which must be taken into account when designing the equipment in terms of efficiency and thermal dissipation. On the other hand, it directly determines the harmonic spectrum at the converter output, facilitating the design of the filters used.
- Reduced ripple (harmonic content): in AC systems it is required that the current and voltage present only a fundamental frequency signal and in DC systems they must present continuous signals. If the harmonic content is too high, it can lead to unwanted effects. For example, in electrical drives, increased losses can be generated in the electrical machine. In applications where the converter is connected to the network, resonances can occur in the system. Having low harmonic content helps to reduce the dimension of the passive elements in the converter (capacitors and inductors).
- Fast dynamic response: Converters are often part of larger systems, where fast power flow changes are required. Therefore a fast dynamic response is needed to fulfill this need.

- Zero tracking error: Standard controllers are designed to follow constant references. However, in alternating current systems, sinusoidal references must be followed. If the current or voltage do not have the stipulated amplitude or phase, undesired effects could occur. For example, if a converter wants to work with unity power factor, this type of error could cause reactive power to be injected or delivered by the converter.

Some of these requirements contradict others, for example a fast dynamic response with low harmonic content. This dependency is of high importance when selecting the control method that effectively meets all or almost all of the aforementioned requirements.

In the last decade, DC/AC power converters (inverters) have been widely used in RE applications as grid interfaces. In wind turbines and photovoltaic systems, inverters are used to connect the generation system to the grid and extract energy from the renewable source to transfer it to the electrical system. In other words, the main objective of the inverter is to control the power delivered to the system, complying with the necessary quality requirements. An additional functionality of this type of converter is that it is possible to control the reactive power delivered or absorbed, without compromising the active power delivered to the grid.

In wind generation systems, the transformation of energy from wind to electricity is done directly in AC, therefore, to connect the generator to the inverter, an AC/DC converter (rectifier) is typically used. This together with the inverter make up the system known as Back-to-Back (BTB) converter. On the other hand, in photovoltaic systems, the transformation of energy occurs in DC, so a DC/DC converter is used to connect the generation to the inverter.

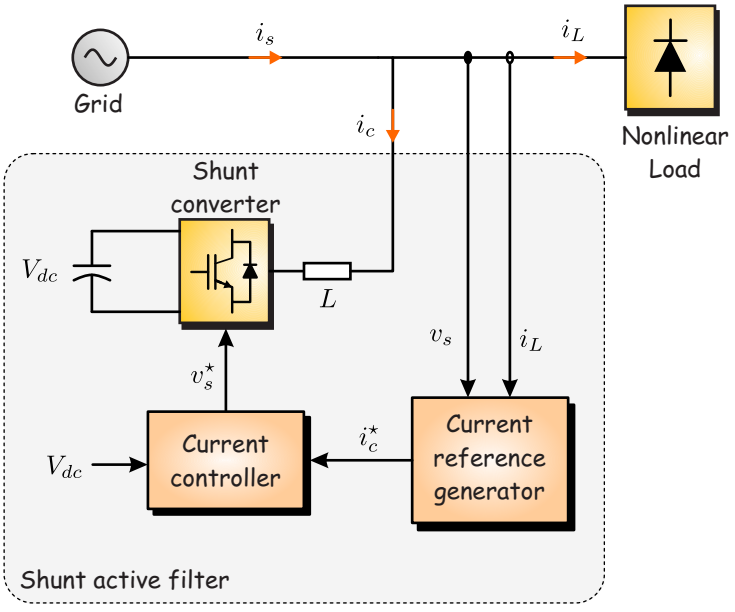

Figure 3.1: Basic interface of shunt active filter.

One of the main uses of inverters is the shunt active filter [28]. The main task of this configuration is to deliver through the inverter all the harmonic currents in the system generated by nonlinear loads reducing the harmonic distortion in the grid allowing to fulfill regulatory requirements. There is no need of connecting an energy source on the DC side of the inverter (like in wind turbine and photovoltaic systems), since it is not used to deliver active power to the system, it only needs to absorb a small amount of energy from the system to maintain the DC voltage constant The reason for this is the inverter is not ideal and it presents power losses mostly because of semiconductor losses. Fig. 3.1 shows a basic diagram of the shunt active filter. The active filter controller can be divided into two parts:

- Current reference generator: The active filter controller is a closed-loop current controller. It needs to continuously sense the load current i_L to compute the instantaneous values of the compensating current reference $i_C^\star$ that will be send to the current controller
- Current controller: Is the part of the controller in charge of synthesize the compensating current calculated by the current reference generator.

The shunt converter needs to work with a high switching frequency f_s in order to reproduce accurately the compensation currents. Normally, $f_s > 10 f_{h_{max}}$, where $f_{h_{max}}$ represents the frequency of the highest order of harmonic current that is going to be compensated [28].

In Fig. 3.1 a voltage-source converter (VSC) is used to represent the shunt converter since almost all shunt active filter in commercial operation use this kind of converter [29]. It can be seen in the figure that the number of wires of the system is not specified. The reason for this is that the power system can be a three-phase three-wire (3P3W) system or a three-phase-four-wire (3P4W) system, the only difference is that the second option considers the neutral wire adding a zero-sequence current to the network. Thus, depending on the characteristics of the system the VSC could be a three-leg or a four-leg converter, so that it can compensate zero-sequence component in addition to harmonic currents if needed [12]. Therefore, the active filter is also capable of compensating reactive current. In this way, the network is only responsible for delivering the active component of the current while any other component will be delivered by the active current filter.

3.2 Current Controllers for Active Filter Applications

The most important element in the control scheme of APF is the current controller. In this kind of applications it is important that the controller achieves good tracking of signals and fast transient response. Generally the deciding criterion when selecting the appropriate control scheme involves an optimal trade-off between cost, complexity and waveform quality needed for meeting international standards requirements. Several

types of controllers have been proposed in literature for APF applications, some of them will be presented below.

3.2.1 Proportional Integral controllers

PI controllers are one of the most widely used controllers in the industry. They are easy to implement and they secure zero steady-state error, but only if signals are constant (which is also known as regulation problem). One accepted solution for tracking sinusoidal references is working in d-q frame, but to do this a method to synchronise with the grid voltage needs to be adopted [30] . However, for APF applications, working in d-q frame is not enough since the controller needs to compensate signals of different frequencies, making it difficult to turn the control problem into a regulation problem.

Shunt active filters are design to compensate harmonic currents, reactive power and zero-sequence currents, so ideally they do not need to absorb or deliver active power to the system. But in practice, power converters have power losses that need to be extracted from some source. If these losses are not compensated then the converter will extract the energy from the DC-link capacitor causing the DC-link voltage to decrease. To avoid this problem, PI controllers are normally adopted to control capacitor voltage levels [12, 31, 32].

3.2.2 Hysteresis controllers

Another simple controller to implement is the hysteresis controller [33]. Every time the error between control references and control variables crosses the predefined boundaries of the hysteresis band, the controller abruptly changes the switching states of the converter keeping the current inside the limits defined by the user. An example of this control scheme is shown in Fig. 3.2. In [34] a hysteresis current controller is used to obtained the gate pulses that command the converter switches, besides, reference generation is computed employing the instantaneous power theory [35]. In [36] hysteresis current control is proposed for Neutral-Point-Clamped (NPC) APF. The proposed control can selectively choose harmonic current components by realtime fast Fourier transform to generate the compensation current. A different proposal is made in [37] where a Fuzzy Hysteresis along with synchronous detection technique controller is developed to control and regulate the DC Capacitor voltage, generation of switching signals and generation of reference currents. Regardless, this type of controller has some disadvantages like variant switching frequency and can generate noise and EMI in the system due to the abrupt switching of the control signal. This can cause interference with other devices and affect the performance of the system.

3.2.3 Poportional Resonant controller

The PI regulation problem evolved to PR controllers allowing the reference tracking in stationary frame at a determined frequency, known as resonant frequency. One advantage that this type of controllers has is that the same controller can be used

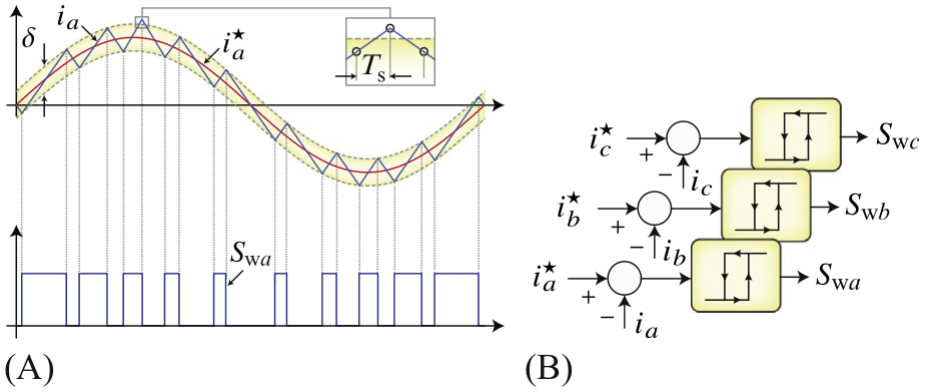

Figure 3.2: An hysteresis current control for a three-phase two-level power converter: (A)operation principle and (B) block diagram.

for three-phase and single-phase systems, something that is not possible with PI controllers because d-q transformation in single-phase systems does not transform the sinusoidal voltages and currents into constant signals. But, in APF cases it becomes necessary to compensate more than one harmonic component of different frequencies. To do this in [38], a simple methodology for designing a single-loop, multiple resonant (MR) controller for simultaneous mitigation of several high-order harmonics, ensuring stability, is presented. The paper [32] proposes the concepts of integrators for sinusoidal signals. A proportional-integral (PI) current controller using stationary-frame generalized integrators is applied for current control of active power filters. Zero steady-state error for the concerned current harmonics is realized, with reduced computation, under unbalanced utility or load conditions. Moreover, [39] presents a hybrid type of controller, called a single synchronous frame hybrid (SSFH) controller, which combines both features: It operates in an SSF mixing conventional PI and resonant controllers. Despite everything mentioned before, one of the most important disadvantages of MR controllers is that they become difficult to tune which makes them prone to stability issues.

3.2.4 Finite Control Set MPC

FCS-MPC has been exhaustible studied over the last few decades [1, 18, 40, 41]. It has also been proposed for APF applications: the work in [12] shows an implementation of a traditional FCS-MPC for a 4L-2L converter analysing simulation and experimental results showing its benefits in this kind of applications. A method based on instantaneous power theory [35] is presented for reference generation of the current controller. Similarly, in [10] where a simple model predictive current control strategy is proposed for four-leg inverters to deliver power to the (un)balanced/(non)linear loads. Unlike classical control schemes, the proposed method does not require current PI controllers or a complex modulation stage. The discrete-time model of the inverter, filter, and load are used to predict the future behavior of the load currents for each of the 16 possible switching states. The control

method chooses a switching state that minimizes the error between the output currents and their references. Furthermore, the work shown in [42] presents a different state feedback approaches of FCS-MPC applied to a grid-connected VSC with an LCL filter. Besides converter-side current feedback, two multivariable control approaches and line-side current control are introduced and compared based on theoretical and experimental evaluation. As the LCL filter introduces an additional resonance frequency to the system, the use of different active damping (AD) methods in combination with FCS-MPC is discussed. Nonetheless, as stated before, the principal drawbacks of FCS-MPC is that it generates a variable switching frequency producing a dispersed harmonic spectrum.

3.3 Current Harmonic Requirements

The integration of renewable sources into the electrical system has been motivated by environmental problems and political and economic incentives. However, this fact means a technical and technological challenge with respect to reliability, stability and power quality of the system. Under this perspective, the impact of the converters connected to the network becomes more significant.

The requirements regarding power quality are mainly focused on maintaining the quality of the network voltage in amplitude, frequency and phase. A voltage disturbance is mainly due to power disturbances (due to the random behavior of some generation sources) or due to transient operations in the system (such as the switching on of high-power induction motors). However, the quality of the current injected into the network is also relevant, and in this sense, the converters connected to the network are responsible for complying with the quality standards imposed by the international [2] and local standards.

The current injected into the network must not have a total harmonic distortion greater than 5%. The Total Demanded Distortion (TDD) is defined as:

$$I_{TDD} = \frac{1}{\sqrt{2} I_{nom}} \sqrt{\sum_{h \neq 1} I_{g,h}^2} \tag{3.1}$$

where I_{nom} corresponds to the rated current of the system and $I_{g,h}$ with $h > 1$ corresponds to the harmonic currents of frequency hf_1. In a three-phase system, the TDD is calculated for each phase and then the values obtained are averaged.

Maximum harmonic current distortion in percent of I_L						
Individual odd harmonic order (odd harmonics)						
I_{sc}/I_L	$2 \leq h < 11$	$11 \leq h < 17$	$17 \leq h < 23$	$23 \leq h < 35$	$35 \leq h < 50$	TDD
< 50	4.0	2.0	1.5	0.6	0.3	5.0
$20 < 50$	7.0	3.5	2.5	1.0	0.5	8.0
$50 < 100$	10.0	4.5	4.0	1.5	0.7	12.0
$100 < 1000$	12.0	5.5	5.0	2.0	1.0	15.0
> 1000	15.0	7.0	6.0	2.5	1.4	20.0

Table 3.1: Table extracted from [2]. Harmonic content limit accepted by the standard for voltage systems between 120 [V] and 69 [kV]

3.4 Description of the 4L-2L VSC

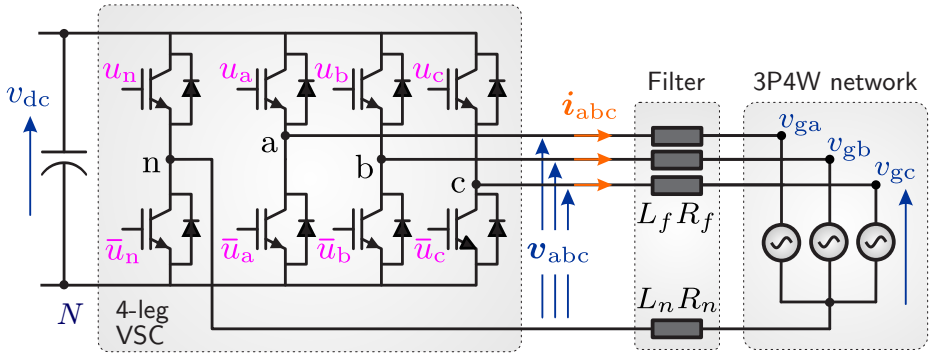

Figure 3.3: Grid-connected 4L-2L VSC.

The circuit diagram of a 4L-2L VSC connected to a 3P4W network through an L-filter is shown in Fig. 3.3. The converter comprises 2 switches in each leg, producing a total of $2^4 = 16$ switching positions $\boldsymbol{u}_{\text{abcn}} \in \{0, 1\}^4$, which are listed in table 3.2. Accordingly, the three-phase output voltage vector can be defined in terms of these switching positions as:

$$\boldsymbol{v}_{\text{abc}} = v_{\text{dc}} \underbrace{\left[u_{\text{a}} - u_{\text{n}}, u_{\text{b}} - u_{\text{n}}, u_{\text{c}} - u_{\text{n}}\right]^{\top}}_{u_{\text{abc}}} \tag{3.2}$$

$$\boldsymbol{T}_{\boldsymbol{\alpha\beta 0}} = \frac{2}{3} \begin{bmatrix} 1 & -\frac{1}{2} & -\frac{1}{2} \\ 0 & \frac{\sqrt{3}}{2} & -\frac{\sqrt{3}}{2} \\ \frac{1}{2} & \frac{1}{2} & \frac{1}{2} \end{bmatrix} \tag{3.3}$$

where $\boldsymbol{u}_{\text{abc}}$ is the three-phase switching state of the converter. Using the amplitude invariant Clarke transform $\mathbf{T}_{\alpha\beta\gamma}$ ((3.3)) [28], it is possible to represent $\boldsymbol{u}_{\text{abc}}$ in the $\alpha\beta\gamma$ framework as:

$$\boldsymbol{u}_{\text{s}} = \begin{bmatrix} u_{\text{s}}^{\alpha} & u_{\text{s}}^{\beta} & u_{\text{s}}^{\gamma} \end{bmatrix}^{\top} = \mathbf{T}_{\alpha\beta\gamma} \boldsymbol{u}_{\text{abc}} \in \mathbb{V} \tag{3.4}$$

Thus, the voltage vector in $\alpha\beta\gamma$ coordinates is $\boldsymbol{v}_{\text{s}} = v_{\text{dc}} \boldsymbol{u}_{\text{s}}$. Fig. 3.4 shows the three-dimensional representation of the 16 switching states in the $\alpha\beta\gamma$ space.

Table 3.2: Switching states of a 4L-2L converter. Voltage values normalized by V_{dc}.

States $[S_a,S_b,S_c,S_n]$	Vectors	u_{an}	u_{bn}	u_{cn}	u_α	u_β	u_γ
0000	$\boldsymbol{u}_{s_0}$	0	0	0	0	0	0
0001	$\boldsymbol{u}_{s_1}$	-1	-1	-1	0	0	-1
0010	$\boldsymbol{u}_{s_2}$	0	0	1	$-1/3$	$-\sqrt{3}/3$	$1/3$
0011	$\boldsymbol{u}_{s_3}$	-1	-1	0	$-1/3$	$-\sqrt{3}/3$	$-2/3$
0100	$\boldsymbol{u}_{s_4}$	0	1	0	$-1/3$	$\sqrt{3}/3$	$1/3$
0101	$\boldsymbol{u}_{s_5}$	-1	0	-1	$-1/3$	$\sqrt{3}/3$	$-2/3$
0110	$\boldsymbol{u}_{s_6}$	0	1	1	$-2/3$	0	$2/3$
0111	$\boldsymbol{u}_{s_7}$	-1	0	0	$-2/3$	0	$-1/3$
1000	$\boldsymbol{u}_{s_8}$	1	0	0	$2/3$	0	$1/3$
1001	$\boldsymbol{u}_{s_9}$	0	-1	-1	$2/3$	0	$-2/3$
1010	$\boldsymbol{u}_{s_{10}}$	1	0	1	$1/3$	$-\sqrt{3}/3$	$2/3$
1011	$\boldsymbol{u}_{s_{11}}$	0	-1	0	$1/3$	$-\sqrt{3}/3$	$-1/3$
1100	$\boldsymbol{u}_{s_{12}}$	1	1	0	$1/3$	$\sqrt{3}/3$	$2/3$
1101	$\boldsymbol{u}_{s_{13}}$	0	0	-1	$1/3$	$\sqrt{3}/3$	$-1/3$
1110	$\boldsymbol{u}_{s_{14}}$	1	1	1	0	0	1
1111	$\boldsymbol{u}_{s_{15}}$	0	0	0	0	0	0

Therein, $\boldsymbol{u}_{s0}$ is the zero vector with single redundancy, and vectors $\boldsymbol{u}_{s1}$ to $\boldsymbol{u}_{s14}$ are the active switching vectors. The space formed by these vectors, highlighted in gray color in Fig. 3.4, represents the control region of the 4L-2L VSC.

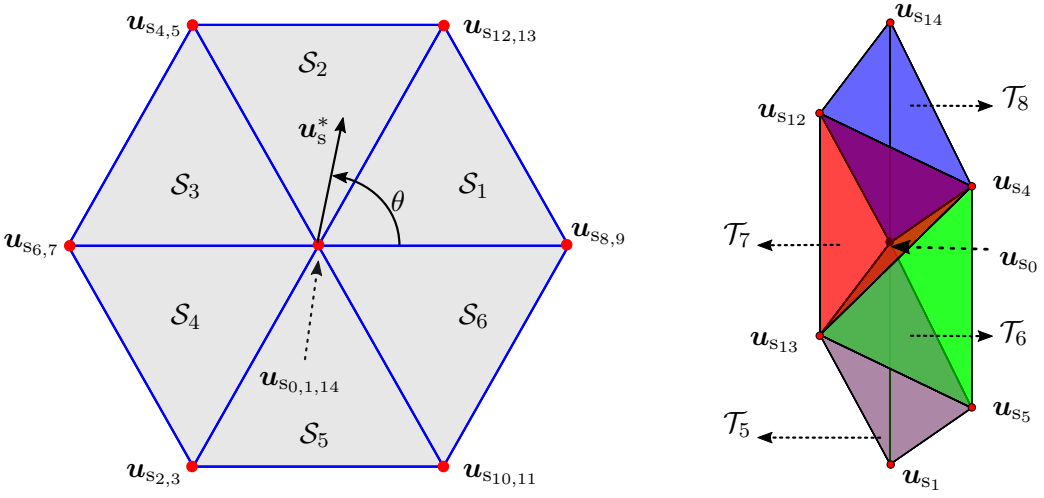

Figure 3.5: (a) Top view of the control region of the 4L-2L-VSI over the $\alpha\beta$ -plane. (b) The four tetrahedra that form the extension of sector $\mathcal{S}_2$ over γ axis (tetrahedron $\mathcal{T}_5$ to $\mathcal{T}_8$)

Fig. 3.5(a) shows a top view of the control region depicted in Fig. 3.4. Like conventional 3-leg 2-level VSCs, the modulation region in $\alpha\beta$ space corresponds to a

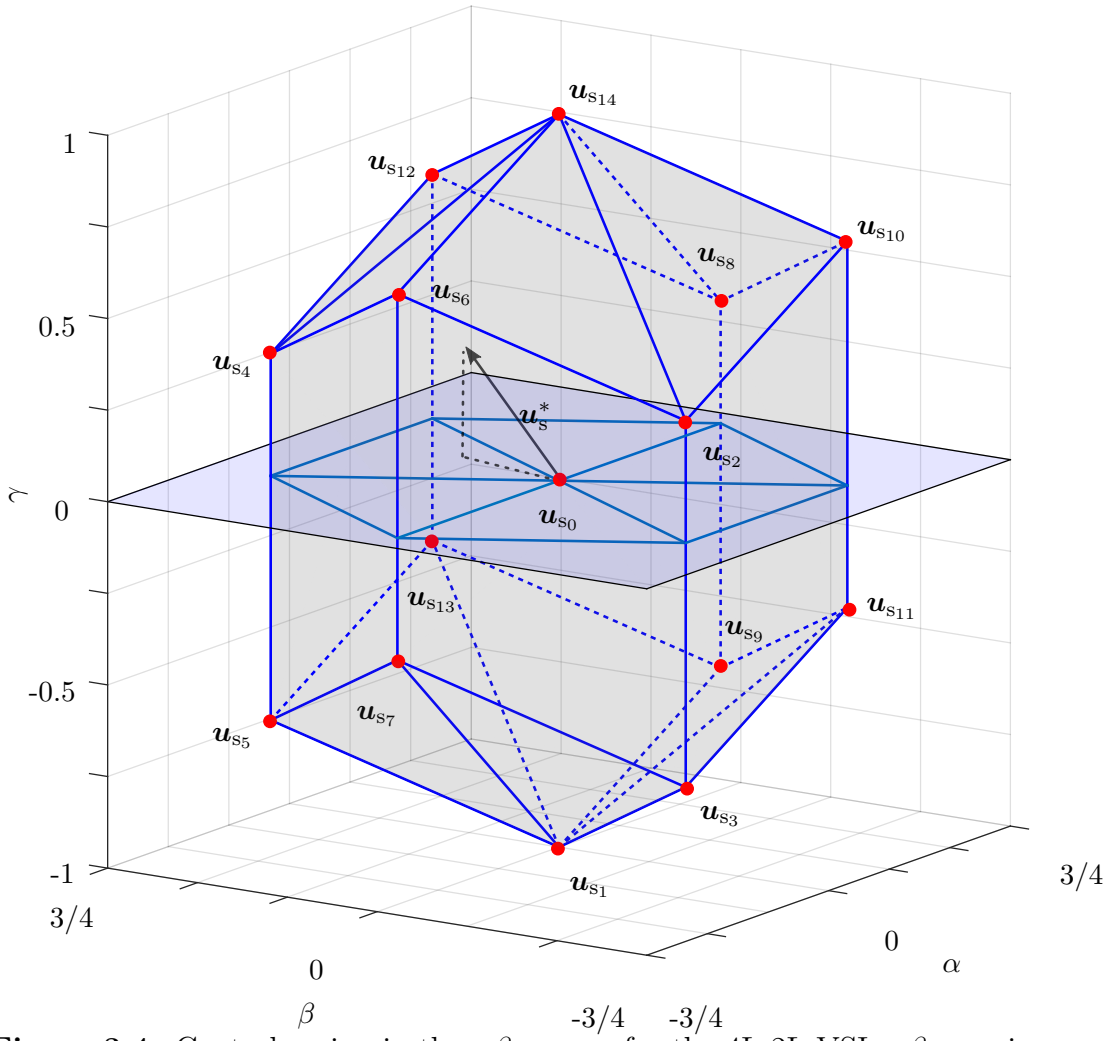

Figure 3.4: Control region in the $\alpha\beta\gamma$ space for the 4L-2L-VSI. $\alpha\beta\gamma$ are in pu

hexagon comprised of six sectors $\mathcal{S}_\ell$ with $\ell \in \{1, \ldots, 6\}$. The enumeration of these sectors is shown in Fig. 3.5. However, in the case of 4L-2L VSCs, each sector can be extended over the γ axis generating 6 pentahedron. For instance, Fig. 3.5(b) shows the pentahedron formed along with sector $\mathcal{S}_2$. Each pentahedron comprises six active vectors and the zero-vector, creating 4 tetrahedra, leading to 24 tetrahedra in the complete region shown in Fig. 3.4. In turns, each tetrahedron is formed by the zero-vector and three active vectors, defining the smallest region where a reference vector can be enclosed. Thereby, in this work, each of the 24 tetrahedra is denoted as: $\mathcal{T}_j(x, y, x)$, where $j \in \mathcal{R} = \{1, \ldots 24\}$, and $\{x, y, x\} \in \Upsilon = \{1, \ldots, 14\}$ indicates the active switching vectors comprising the jth tetrahedron. In this work, the tetrahedra are sequentially enumerated from the bottom to the top of pentahedron $\mathcal{S}_\ell$ as $j = 4(\ell - 1) + \kappa$, where $\kappa \in \{1, \ldots, 4\}$. In table A.1 shown in the appendix all sectors are enumerated with their respective tetrahedrons and vectors.

To synthesize a desired output voltage, the four nearest switching vectors are commonly employed in carrier-based and space vector PWM techniques for 4-leg

inverter, which are arranged in a specific switching sequence [43]. Discontinuous seven-segment switching sequence (7S-SS), using only one redundancy of the zero vector (either $\boldsymbol{u}_{\mathrm{s_{0N}}}$ or $\boldsymbol{u}_{\mathrm{s_{0P}}}$), can be implemented to reduce switching frequency at the cost of more harmonic distortion. Symmetrical nine-segment switching sequences 9S-SS can be also implemented using both redundancies of the zero vector, improving the harmonic spectrum of the synthesized waveforms, at the cost of higher switching commutation. Fig. 4.2 shows the symmetrical 9S-SS for tetrahedron $\mathcal{T}_7(4, 12, 13)$.

Chapter 4

Proposed Optimal Switching Sequence MPC Strategy

In this chapter the proposed OSS-MPC strategy will be formulated. To do so, the procedure is developed in several steps. First, the continuous-time model of the system is obtained. After this, the discrete model is achieved in order to obtain the model prediction of the system. Next, the cost function is formulated. This will allow to obtain the equations to compute the duty cycles or time application of the vectors. Also, an algorithm is shown to calculate the duty cycles in cases of over-modulation. After this, the algorithm to define the optimal solution is defined, proposing a method that will reduce the computational burden. The following section explains the tuning of the controller and how it is manipulated to change the dynamics of the system. Afterwards, it is explained how the modulating signals (that will be compared with the carrier signal) are computed. Finally, some tools that were used to achieve a better performance of the proposed method are presented and explained (Kalman filter and compensation of future references).

4.1 OSS-MPC for 4-Leg Grid-Tied Converters

4.1.1 Continuous-Time Model

To formulate the control strategy, the continuous-time model of the system shown in Fig. 4.1 is expressed in $\alpha\beta\gamma$ coordinates as:

$$\frac{\mathrm{d}\boldsymbol{i}_\mathrm{g}}{\mathrm{d}t} = -\mathbf{L}^{-1}\mathbf{R}\boldsymbol{i}_\mathrm{g} - \mathbf{L}^{-1}\boldsymbol{v}_\mathrm{g} + \mathbf{L}^{-1}v_\mathrm{dc}\boldsymbol{u}_\mathrm{s} \tag{4.1}$$

where $\boldsymbol{i}_\mathrm{g} = \begin{bmatrix} i_\mathrm{g}^\alpha & i_\mathrm{g}^\beta & i_\mathrm{g}^\gamma \end{bmatrix}^\intercal$ and $\boldsymbol{v}_\mathrm{g} = \begin{bmatrix} v_\mathrm{g}^\alpha & v_\mathrm{g}^\beta & v_\mathrm{g}^\gamma \end{bmatrix}^\intercal$ are the grid current and voltage vectors, respectively. In (4.1), the matrices are defined as:

$$\mathbf{L} = \begin{bmatrix} L_f & 0 & 0 \\ 0 & L_f & 0 \\ 0 & 0 & L_\gamma \end{bmatrix} \quad \mathbf{R} = \begin{bmatrix} R_f & 0 & 0 \\ 0 & R_f & 0 \\ 0 & 0 & R_\gamma \end{bmatrix} \tag{4.2}$$

being L_γ=L_f+3L_n and R_γ=R_f+3R_n, the zero-sequence inductance and resistance, respectively.

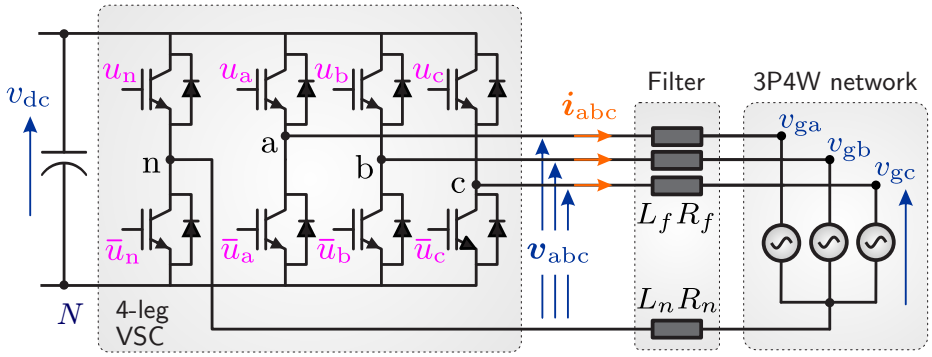

Figure 4.1: Grid-connected 4L-2L VSC.

4.1.2 Discrete-Time Model: The Average Trajectory

Typically in FCS-MPC strategies applied to 4-leg inverters [10, 12, 44, 45], the optimal switching action is obtained from minimizing a cost function capturing the instantaneous tracking error of the grid currents along with the switching effort (to control the switching frequency indirectly). Consequently, the closed-loop performance depends on the weighting factor choice, which is not trivial to perform [46, 47]. This work proposes tracking the average trajectory of the grid currents (over the switching cycle T_s) by adequately manipulating the application times of the switching vectors comprised in the 9S-SS (nine-segment switching sequence) [48]. Thus, the average tracking error is improved by the proposed controller. Moreover, the subsequent modulation stage, used to synthesize the desired switching sequence, fixes the switching frequency, avoiding the use of a weighting factor and resulting in deterministic switching losses.

For modeling the grid current average trajectory over one switching period T_p, two assumptions are made. First, the interval T_s is considerably smaller than the shortest time constant of the system, i.e., $T_p \ll L_f/R_f$. Accordingly, when the converter applies a given 9S-SS, the grid current $\boldsymbol{i}_g(t)$ evolves linearly over each subinterval t_i, where the subscript i indicates the instant at which the converter changes from one state to another, i.e., as illustrated in Fig. 4.3, $t_1 = d_{0_N}$, $t_2 = d_x$, $t_3 = d_y$, $t_4 = d_z$, and $t_5 = d_{0_P}$ where $d_i = t_i/T_p$. Hence, the trajectory can be considered as a piecewise linear function of the time, as shown in Fig. 4.3. Thus, by employing the Forward Euler method:

$$x(k+1) = x(k) + \Delta t \frac{dx}{dt} \tag{4.3}$$

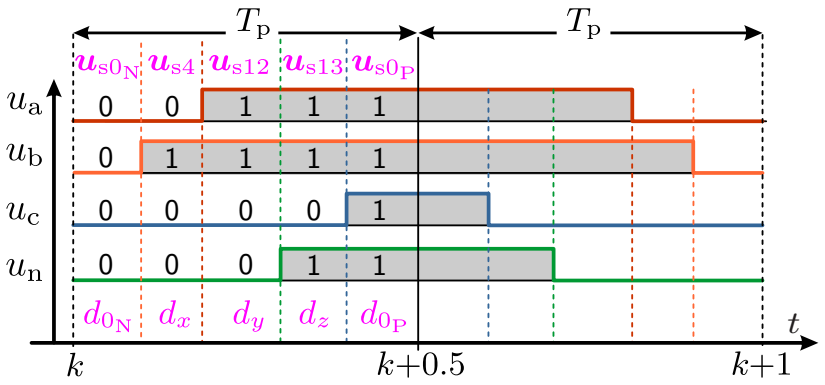

Figure 4.2: Symmetrical 9S-SS for the tetrahedron $\mathcal{T}_7(4, 12, 13)$.

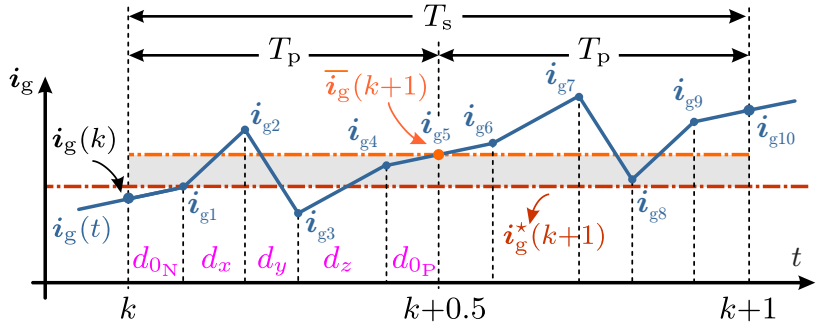

Figure 4.3: Predicted system trajectory for a 9S-SS.

the instantaneous evolution of $\boldsymbol{i}_g$ can be sequentially computed as

$$\boldsymbol{i}_{g(i+1)} = \boldsymbol{i}_{g(i)} + \left.\frac{d\boldsymbol{i}_g}{dt}\right|_i T_p d_i \tag{4.4}$$

where $d_i = t_i/T_p \in \mathbb{D} \triangleq [0, 1]$ is the normalized application time (duty cycle), and $T_p{=}T_s/2$ is the sub-cycle period. Besides, due to the symmetrical nature of the 9S-SS, the instant value of the grid current in the middle of the sampling period $\boldsymbol{i}_g(k{+}0.5) = i_{g5}$, is equal to the average value of the current $\overline{\boldsymbol{i}_g}(k+1)$ in the interval time of T_s, i.e., $\overline{\boldsymbol{i}_g}(k+1) = i_{g5}$. Thus, it is expressed as:

$$\overline{\boldsymbol{i}_g}(k+1) = \boldsymbol{i}_g(k) + T_p \sum_{i\in\mathcal{I}} \left.\frac{d\boldsymbol{i}_g}{dt}\right|_i d_i, \quad \mathcal{I} = \{0_N, x, y, z, 0_P\} \tag{4.5}$$

Then, by using the continuous model of the system 4.1, the ith subinterval slope can be defined as:

$$\left.\frac{d\boldsymbol{i}_g}{dt}\right|_i = -\mathbf{L}^{-1}\mathbf{R}\boldsymbol{i}_{g(i)} - \mathbf{L}^{-1}\boldsymbol{v}_{g(i)} + \mathbf{L}^{-1}v_{dc}\boldsymbol{u}_{s(i)} \tag{4.6}$$

Finally, it is assumed that the fundamental period of the grid voltages is much higher than T_p. Then, every sub-interval gradient, i.e., $\left.\frac{d\boldsymbol{i}_g}{dt}\right|_i$, is computed using the system variables sampled values at instant k, i.e., $\boldsymbol{v}_{g(i)} = \boldsymbol{v}_g(k)$ and $\boldsymbol{u}_{s(i)} = \boldsymbol{u}_s(k)$

$\forall i \in \mathcal{I}$. Accordingly, by substituting (4.6) in (4.5) and introducing the duty cycle vector $\boldsymbol{d}(k)$ and switching matrix $\boldsymbol{U}(k)$ defined as:

$$\boldsymbol{d}(k) \triangleq \begin{bmatrix} d_0(k) & d_x(k) & d_y(k) & d_z(k) \end{bmatrix}^{\intercal} \in \mathbb{D}^4, \tag{4.7}$$

$$\boldsymbol{U}(k) \triangleq \begin{bmatrix} \boldsymbol{u}_{\mathrm{s}0}(k) & \boldsymbol{u}_{\mathrm{s}x}(k) & \boldsymbol{u}_{\mathrm{s}y}(k) & \boldsymbol{u}_{\mathrm{s}z}(k) \end{bmatrix}, \tag{4.8}$$

the average trajectory (4.5) can be expressed as:

$$\overline{\boldsymbol{i}_{\mathrm{g}}}(k+1) = \mathbf{A}\boldsymbol{i}_{\mathrm{g}}(k) + \mathbf{P}\boldsymbol{v}_{\mathrm{g}}(k) + \mathbf{B}\boldsymbol{U}(k)\boldsymbol{d}(k) \tag{4.9}$$

with $\mathbf{A} = (\mathbf{I} - \mathbf{L}^{-1}\mathbf{R}T_{\mathrm{p}})$, $\mathbf{P} = -T_{\mathrm{p}}\mathbf{L}^{-1}$, $\mathbf{B} = v_{\mathrm{dc}}T_{\mathrm{p}}\mathbf{L}^{-1}$, $d_0 \triangleq d_{0_{\mathrm{P}}} + d_{0_{\mathrm{N}}}$ and $\boldsymbol{u}_0 \triangleq \boldsymbol{u}_{\mathrm{s}0_{\mathrm{P}}} = \boldsymbol{u}_{\mathrm{s}0_{\mathrm{N}}}$.

Unlike the OSS-MPC strategies for 3-leg VSCs (e.g., [26] [49] [50]), the duty cycle vector $\boldsymbol{d}$ has four components and every switching sequence is defined by 4 switching vectors in matrix $\boldsymbol{U}$. Hence, the average switching vector applied by the converter is given by $\boldsymbol{u}(k) = \boldsymbol{U}(k)\boldsymbol{d}(k)$.

For the sake of simplicity, hereinafter $\overline{\boldsymbol{i}_{\mathrm{g}}}(k+1)$ will be denoted as $\boldsymbol{i}_{\mathrm{g}}(k+1)$; and therefore, (4.9) will be considered as the discrete-time model.

4.1.3 Optimal Control Problem

To obtain the optimum duty cycles for each of the 24 possible switching sequences $\boldsymbol{S}_j(\boldsymbol{U}_j, \boldsymbol{d}_j)$, the following objective function is introduced:

$$J_j = \left\| \boldsymbol{i}_{\mathrm{g}}(k+1) - \boldsymbol{i}^*_{\mathrm{g}}(k+1) \right\|_2^2 + \left\| \boldsymbol{\Lambda}_u \left(\boldsymbol{U}_j\boldsymbol{d}_j - \boldsymbol{u}_{\mathrm{ss}}(k) \right) \right\|_2^2, \tag{4.10}$$

This quadratic cost function is formulated to quantify two control objectives: the average tracking error and the control effort. The diagonal matrix $\boldsymbol{\Lambda}_u = \mathrm{diag}(\lambda_u^{\alpha}, \lambda_u^{\beta}, \lambda_u^{\gamma})$ is used to adjust the compromise between both control objectives, avoiding the proposed OSS-MPC behaving like a deadbeat controller because this may produce robustness issues [17].

Indeed, by substituting (4.9) into (4.10), the cost function can be rewritten in the following equivalent form:

$$J_j = \left\| \mathbf{B} \left(\boldsymbol{U}_j\boldsymbol{d}_j - \boldsymbol{u}_{\mathrm{db}}(k) \right) \right\|_2^2 + \left\| \boldsymbol{\Lambda}_u \left(\boldsymbol{U}_j\boldsymbol{d}_j - \boldsymbol{u}_{\mathrm{ss}}(k) \right) \right\|_2^2, \tag{4.11}$$

where $\boldsymbol{u}_{\mathrm{db}}(k)$ is the deadbeat control input defined as

$$\boldsymbol{u}_{\mathrm{db}}(k) = \mathbf{B}^{-1} \left(\boldsymbol{i}^{\star}_{\mathrm{g}}(k+1) - \mathbf{A}\boldsymbol{i}_{\mathrm{g}}(k) - \mathbf{P}\boldsymbol{v}_{\mathrm{g}}(k) \right) \tag{4.12}$$

Moreover, in the second term of (4.11), the signal $\boldsymbol{u}_{\mathrm{ss}}(k)$ is the control input that

ensures the output currents track their references under ideal conditions in which both the disturbances and system parameters are certainly known [17, 26]. Thus, $\boldsymbol{u}_{\mathrm{ss}}(k)$ refers to open-loop or steady-state control input, and it is determined from (4.1) as:

$$\boldsymbol{u}_{\mathrm{ss}}(k) = \frac{1}{v_{\mathrm{dc}}(k)} \left(\mathbf{L} \frac{\mathrm{d}\boldsymbol{i}_{\mathrm{g}}^{*}(k)}{\mathrm{d}t} + \mathbf{R}\boldsymbol{i}_{\mathrm{g}}^{*}(k) + \boldsymbol{v}_{\mathrm{g}}(k) \right) \tag{4.13}$$

Therefore, by inspecting (4.11), it is shown that the positive definite matrix $\boldsymbol{\Lambda}_u$ allows the dynamic response and robustness properties of the closed-loop system to be modified [24]. Further details on the methodology used to design the parameters of the tuning matrix $\boldsymbol{\Lambda}_u$ will be presented in section 4.1.6.

On the other hand, as described in (4.11), for every tetrahedron $j \in \mathcal{R}$, the cost function is expressed as a function of the matrix $\boldsymbol{U}_j$ and the normalized application times $\boldsymbol{d}_j$. Consequently, the OSS is obtained by solving, at each sampling period k, the following OSS-MPC problem [51]:

$$\boldsymbol{S}_{\mathrm{op}} = \arg\min_{\boldsymbol{U}_j} \Big\{ \min_{\boldsymbol{d}_j} \; J(\boldsymbol{d}_j, \boldsymbol{U}_j) \Big\} \tag{4.14a}$$

$$\text{s.t.} \;\; \mathbb{1}^{\intercal} \boldsymbol{d}_j = 1 \tag{4.14b}$$

$$\boldsymbol{d}_j \geq 0 \tag{4.14c}$$

It is worth highlighting that the optimal control problem underlying the OSS-MPC (4.14) considers two nested optimizations. First, in the internal optimization step, a local minimal solution $\boldsymbol{d}_j$ is obtained for the jth switching sequence candidate (where $j \in \mathcal{R}$). Then, in the external optimization stage, the pair $\{\boldsymbol{U}^{\star}, \boldsymbol{d}^{\star}\}$ providing the minimum cost function value defines the OSS, namely $\boldsymbol{S}_{\mathrm{op}}$.

4.1.4 Duty Cycles Calculation

To solve the OSS-MPC problem (4.14), it is proposed first to compute the relaxed solution to the inner optimization stage. To this end, constraint $\boldsymbol{d}_j \geq 0$ is ignored, and thus, the relaxed solution, namely $\boldsymbol{d}_{\mathrm{r}}$, is the one that solves the following bi-objective constrained least-square problem,

$$\begin{aligned} \min_{\boldsymbol{d}_{\mathrm{r}j}} \;\; & \left\| \mathbf{B}(\boldsymbol{U}_j \boldsymbol{d}_{\mathrm{r}j} - \boldsymbol{u}_{\mathrm{db}}) \right\|_2^2 + \left\| \boldsymbol{\Lambda}_u (\boldsymbol{U}_j \boldsymbol{d}_{\mathrm{r}j} - \boldsymbol{u}_{\mathrm{ss}}) \right\|_2^2 \\ \text{s.t.} \;\; & \mathbb{1}^{\intercal} \boldsymbol{d}_{\mathrm{r}j} = 1. \end{aligned} \tag{4.15}$$

Thereby, using the Lagrange multipliers, the solution to (4.15) for every switching sequence candidate is given by:

$$\boldsymbol{d}_{\mathrm{r}j}(k) = \begin{bmatrix} \boldsymbol{U}_j \\ \mathbb{1}^{\top} \end{bmatrix}^{-1} \begin{bmatrix} \boldsymbol{u}_{\mathrm{uc}}(k) \\ 1 \end{bmatrix} \tag{4.16}$$

where $\boldsymbol{u}_{\mathrm{uc}}(k)$ is the unconstrained average switching vector (UASV) defined as:

$$\boldsymbol{u}_{\mathrm{uc}}(k) = \left(\mathbf{B}^{\top}\mathbf{B} + \boldsymbol{\Lambda}_u^{\top}\boldsymbol{\Lambda}_u\right)^{-1}\left(\mathbf{B}^{\top}\mathbf{B}\boldsymbol{u}_{\mathrm{db}}(k) + \boldsymbol{\Lambda}_u^{\top}\boldsymbol{\Lambda}_u\boldsymbol{u}_{\mathrm{ss}}(k)\right) \tag{4.17}$$

Thus, by using (4.8) into (4.16), the relaxed solution associated with the jth switching sequence candidate is computed by using the closed-form solution in (4.18). Therein, only the $\alpha\beta\gamma$ components of both the UASV, $\boldsymbol{u}_{\mathrm{uc}}(k)$, and the switching vectors comprising every switching sequence, $\{\boldsymbol{u}_{xj}, \boldsymbol{u}_{yj}, \boldsymbol{u}_{zj}\}$, are needed to calculate the relaxed duty cycles.

$$\Theta_j = u_{xj}^{\alpha}u_{yj}^{\gamma}u_{zj}^{\beta} - u_{xj}^{\alpha}u_{yj}^{\beta}u_{zj}^{\gamma} + u_{xj}^{\beta}u_{yj}^{\alpha}u_{zj}^{\gamma} - u_{xj}^{\beta}u_{yj}^{\gamma}u_{zj}^{\alpha} - u_{xj}^{\gamma}u_{yj}^{\alpha}u_{zj}^{\beta} + u_{xj}^{\gamma}u_{yj}^{\beta}u_{zj}^{\alpha} \tag{4.18a}$$

$$d_{\mathrm{r}xj} = \frac{1}{\Theta_j}\Big(u_{\mathrm{uc}}^{\alpha}(u_{yj}^{\gamma}u_{zj}^{\beta} - u_{yj}^{\beta}u_{zj}^{\gamma}) + u_{\mathrm{uc}}^{\beta}(u_{yj}^{\alpha}u_{zj}^{\gamma} - u_{yj}^{\gamma}u_{zj}^{\alpha}) + u_{\mathrm{uc}}^{\gamma}(u_{yj}^{\beta}u_{zj}^{\alpha} - u_{yj}^{\alpha}u_{zj}^{\beta})\Big) \tag{4.18b}$$

$$d_{\mathrm{r}yj} = \frac{1}{\Theta_j}\Big(u_{\mathrm{uc}}^{\alpha}(u_{xj}^{\beta}u_{zj}^{\gamma} - u_{xj}^{\gamma}u_{zj}^{\beta}) + u_{\mathrm{uc}}^{\beta}(u_{xj}^{\gamma}u_{zj}^{\alpha} - u_{xj}^{\alpha}u_{zj}^{\gamma}) + u_{\mathrm{uc}}^{\gamma}(u_{xj}^{\alpha}u_{zj}^{\beta} - u_{xj}^{\beta}u_{zj}^{\alpha})\Big) \tag{4.18c}$$

$$d_{\mathrm{r}zj} = \frac{1}{\Theta_j}\Big(u_{\mathrm{uc}}^{\alpha}(u_{xj}^{\gamma}u_{yj}^{\beta} - u_{xj}^{\beta}u_{yj}^{\gamma}) + u_{\mathrm{uc}}^{\beta}(u_{xj}^{\alpha}u_{yj}^{\gamma} - u_{xj}^{\gamma}u_{yj}^{\alpha}) + u_{\mathrm{uc}}^{\gamma}(u_{xj}^{\beta}u_{yj}^{\alpha} - u_{xj}^{\alpha}u_{yj}^{\beta})\Big) \tag{4.18d}$$

$$d_{\mathrm{r}0j} = 1 - d_{\mathrm{r}xj} - d_{\mathrm{r}yj} - d_{\mathrm{r}zj} \tag{4.18e}$$

However, it is worth highlighting that the solution in (4.18) does not necessarily satisfy the non-negative constraint (4.14c). Thus, unfeasible solutions could be provided by the controller under some operating conditions. Specifically, during transients, the vector $\boldsymbol{u}_{\mathrm{uc}}(k)$ could be fallen outside the control region shown in Fig. 3.4. On that condition, the application time for the null switching vectors must be negative ($d_0 < 0$) to compensate for the over-application of the active switching vectors. To provide feasible solutions, the duty cycle vector is computed from the relaxed one $\boldsymbol{d}_{\mathrm{r}j}$ as:

$$\boldsymbol{d}_j = \frac{\boldsymbol{d}_{\mathrm{r}j}^{+}}{\mathbb{1}^{\top}\boldsymbol{d}_{\mathrm{r}j}^{+}} \tag{4.19}$$

where $\boldsymbol{d}_{\mathrm{r}j}^{+} = \max(0, \boldsymbol{d}_{\mathrm{r}j})$ leads to the non-negative values of $\boldsymbol{d}_{\mathrm{r}j}$. Notice that the relaxed solution given in (4.19) is the optimal application times under steady-state operation since $\boldsymbol{d}_{\mathrm{r}j}^{+} = \boldsymbol{d}_{\mathrm{r}j}$ and $\mathbb{1}^{\intercal}\boldsymbol{d}_{\mathrm{r}j} = 1$. However, depending on the closed-loop dynamic achieved by the proposed OSS-MPC, the controller can lead to suboptimal solutions during transients.

As a result of transient conditions, when a change in reference value occurs, the controller will normally require the converter to apply large actuation values that are outside of the polyhedron or control region presented in Fig. 3.4. The resulting u_{uc} vector needs to be synthesized with a linear combination of the null-vector u_{s0} and

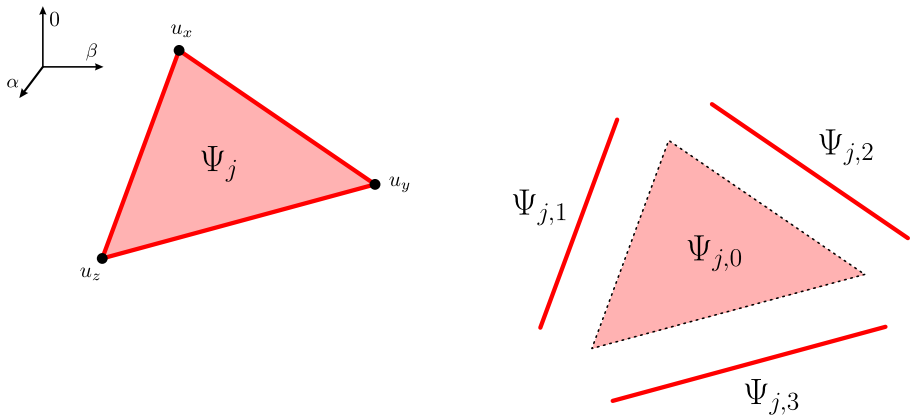

Figure 4.4: Subregions of the outer face of every tetrahedron

the three active vectors u_{sx}, u_{sy}, u_{sz}, but the converter will not be able to deliver the desired output voltage. Constraint (4.14b) represents this physical limitation of the converter. To fulfill with the constraints of the problem the solution in this cases must be located in the outer face of the control region, or more specifically, of one of the tetrahedra. Fig. 4.4 shows the outer face of jth tetrahedron. The method proposed in (4.19) satisfies this restriction but it does not minimize the objective function (4.10). As can be seen in Fig. 4.4 the region Ψ_j can be synthesized using only a linear combination of the three active vectors d_x, d_y, d_z, so immediately can be assumed that the application time of null-vector is equal to zero, $d_0 = 0$, decreasing the number of variables to be found.

In mathematical optimization problems the region Ψ_j is classified as a convex set, because every line segment between any two points in Ψ_j lies in Ψ_j. In convex optimization problems exists a method to solve Quadratic Problems (QP) with linear inequality constraints called Active-Set Method (ASM) [52]. The main idea of the ASM is to reduce the inequality constraint QP problem (due to the no negative constraint of the application times) to a sequence of equality constraint QP problems that can be solved using the techniques like the one described in section 4.1.4. In other words, the region Ψ_j can be divided into four sub-regions $\Psi_{j,i}$ where $i = \{0, 1, 2, 3\}$, and $d_0 = 0$ to compute the relaxed solution for each of them. This method will be developed as a novel contribution to this work allowing to solve the optimal solution of the optimal problem defined in (4.14) for every case.

4.1.5 Cost function minimization and OSS selection

Since the controller can calculate the duty cycle vector for every switching sequence candidate using (4.18) and (4.19), the optimal one needs to be further selected to determine the OSS. If computationally feasible, this task can be done by exhaustively enumerating all candidate solutions using the same working principle of the standard FCS-MPC strategy (e.g., [49,53]). It means that the cost function (4.11) must be computed for all switching sequence candidates $j \in \mathcal{R}$ using the duty cycles

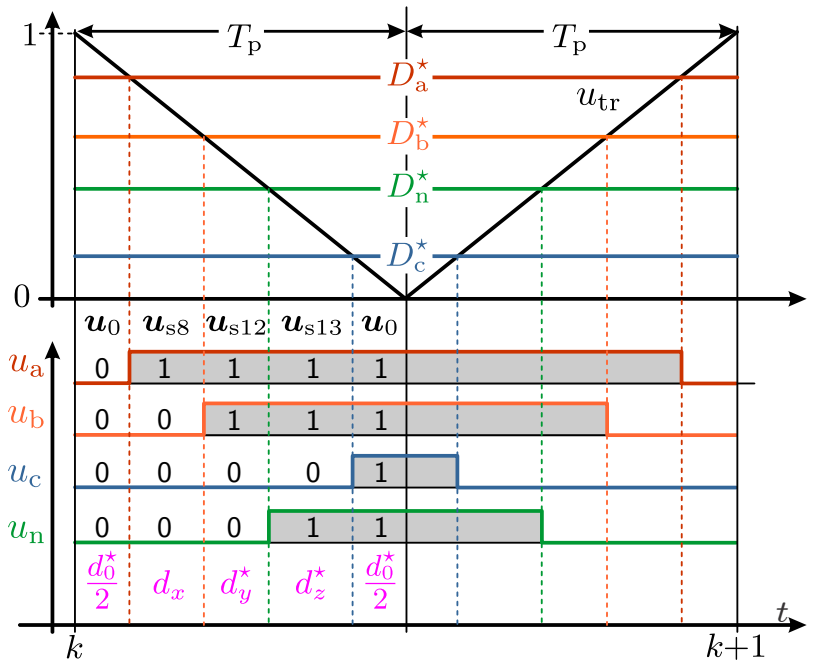

Figure 4.5: Single-carrier-based PWM to synthesize the desired SS.

$\boldsymbol{d}_j$ firstly calculated from (4.18) and (4.19). Thus, the index with the minimal cost function value, namely j_{op}, defines the optimal switching sequence $\boldsymbol{S}_{\text{op}} = \left\{\boldsymbol{d}^\star, \boldsymbol{U}^\star\right\}$.

Aiming to reduce the computational burden, in this work, the OSS-MPC algorithm introduced in [26] for 3L-NPC converters is adapted for 4L-2L grid-connected converters. To this end, since every sector comprises 4 tetrahedra (see Fig. 3.5), the first step is to determine the sector in which $\boldsymbol{u}_{\text{uc}}(k)$ is projected on the $\alpha\beta$-plane (namely $\mathcal{S}_{\ell_{\text{op}}}$) as:

$$\ell_{\text{op}} = \text{ floor } \left\{\frac{3}{\pi}\tan^{-1}\left(\frac{u_{\text{uc}}^{\beta}}{u_{\text{uc}}^{\alpha}}\right)\right\} + 1. \tag{4.20}$$

Then, the duty cycle vector $\boldsymbol{d}_j$ is computed only for the four tetrahedra within $\mathcal{S}_{\ell_{\text{op}}}$, i.e., for $j = 4(\ell_{\text{op}} - 1) + \kappa$, with $\kappa \in \{1, \ldots 4\}$. Consequently, using (4.17) and (4.20), the conventional enumeration algorithm for which the closed-form solution (obtained from (4.18) and (4.19)) is evaluated can be reduced from 24 to only 4, certainly reducing the computational overhead of the control algorithm.

4.1.6 Tuning of the controller

The design of the tuning matrix $\boldsymbol{\Lambda}_u$ is straightforward. As shown in (4.17), $\boldsymbol{u}_{\text{uc}}(k)$ is the weighted sum between the deadbeat and the steady-state control inputs. It follows that by choosing $\boldsymbol{\Lambda}_u = \mathbf{B}$, the resulting control action will put the same priority to the grid current tracking error and control effort. Thus, using a large tuning matrix $\boldsymbol{\Lambda}_u$ compared with $\mathbf{B}$, the converter will apply an average switching vector close to $\boldsymbol{u}_{\text{ss}}(k)$, which leads to open-loop operation. Conversely, if $\boldsymbol{\Lambda}_u \approx 0$, the

first term in the cost function (4.11) becomes predominant and, hence, the converter tends to synthesize the deadbeat control action $\boldsymbol{u}_{\mathrm{db}}(k)$ in (4.12), which increases the controller bandwidth. Consequently, by starting from the initial setting point given by $\boldsymbol{\Lambda}_{u0} = \mathbf{B}$, i.e.,

$$\Lambda_{u0} = \mathrm{diag}\left(\lambda_{u0}^{\alpha}, \lambda_{u0}^{\beta}, \lambda_{u0}^{\gamma}\right) = V_{\mathrm{dc}} T_{\mathrm{p}}\, \mathrm{diag}\left(L_f^{-1}, L_f^{-1}, L_{\gamma}^{-1}\right) \tag{4.21}$$

the tuning parameters $\lambda_u^{\alpha\beta\gamma}$ can be manipulated in order to reduce ($\lambda_u^{\alpha\beta\gamma} > \lambda_{u0}^{\alpha\beta\gamma}$) or increase ($\lambda_u^{\alpha\beta\gamma} < \lambda_{u0}^{\alpha\beta\gamma}$) the closed-loop dynamic. Notice that this controller setting allows one to tune the dynamic behavior of the grid current's $\alpha\beta\gamma$ components in a decoupled manner. This implies that, for instance, the proposed controller can regulate the positive-, negative-, and zero-sequence components of the grid currents with different closed-loop dynamics.

4.1.7 OSS Implementation

Aiming to determine the modulating signals $\boldsymbol{D}^{\star}_{\mathrm{abcn}} = \left[D^{\star}_{\mathrm{a}}\, D^{\star}_{\mathrm{b}}\, D^{\star}_{\mathrm{c}}\, D^{\star}_{\mathrm{n}}\right]^{\intercal} \in [0,1]^4$ that allow the converter to synthesize the desired OSS, namely $\boldsymbol{S}_{\mathrm{op}}$, the method introduced in [54] is adopted in this work. Thus, the desired modulating signals are computed according to:

$$\boldsymbol{D}^{\star}_{\mathrm{abcn}} = d_x^{\star}\boldsymbol{u}^{\star}_{\mathrm{abcn},x} + d_y^{\star}\boldsymbol{u}^{\star}_{\mathrm{abcn},y} + d_z^{\star}\boldsymbol{u}^{\star}_{\mathrm{abcn},z} + \frac{1}{2}d_0^{\star} \tag{4.22}$$

where $\boldsymbol{u}^{\star}_{\mathrm{abcn},\Upsilon}$ are the 4-leg switching positions that produce the active switching vectors comprising the optimal tetrahedron j_{op}. Fig. 4.5 shows an illustrative example of this method when the optimal tetrahedron is $\mathcal{T}_{j_{\mathrm{op}}} = (8, 12, 13)$. Note that, using this simple OSS implementation, the carrier-signal frequency imposes the switching frequency of the converter's semiconductors.

4.1.8 Kalman filter

During the experimental tests, it was possible to appreciate that the controller was sensitive to the parameters of the system influencing in the steady-state performance of the controller. For this reason, a Kalman filter is implemented [55]. The Kalman filter is in other words a closed-loop observer. It can be used to estimate state variables, but in this case, it is applied to filter the current signal $\boldsymbol{i}_g$ that is being measured. This kind of observer has a discrete nature, thus, the discrete model of the system needs to be used (equation (4.9)). Kalman filter implementation consists in adding to the discrete model the product of the error of the state estimation $\boldsymbol{e}(k) = \boldsymbol{x}(k) - \hat{\boldsymbol{x}}(k)$ and a gain $\mathbf{K}$ (in this case $\boldsymbol{x}(k) = \boldsymbol{i}_g(k)$ and $\hat{\boldsymbol{x}}(k) = \hat{\boldsymbol{i}}_g(k)$), thus:

$$\hat{\boldsymbol{i}}_{\mathrm{g}}(k{+}1) = \mathbf{A}\hat{i}_{\mathrm{g}}(k) + \mathbf{P}\boldsymbol{v}_{\mathrm{g}}(k) + \mathbf{B}\,\boldsymbol{u}_s(k) + \mathbf{K}e(k) \tag{4.23}$$

where $\mathbf{K} > 0$ is the only restriction to assure the convergence of the estimated variables. The value of the gain $\mathbf{K}$ is obtained by solving the Riccati's equation [55]. The advantage of using this kind of observer is that the estimated states correspond

to the predicted variables as can be seen in (4.23). Therefore, this observer is used instead of equation (4.9). To avoid using extra processing time, the gain **K** is computed offline using the solver *idare* of MATLAB.

4.1.9 Computation of future references and grid voltage

As a consequence of the discrete nature of digital platforms and predictive control schemes [56] it becomes necessary to predict future grid-voltage values for two main reasons. First, to make the right prediction of the future current and second to avoid the delay generation in current reference. To do this two methods are used:

4.1.9.1 Vector angle compensation

In steady state, it can be assumed that the vector rotates at a constant angular speed ω and that the magnitude remains constant. In this way, the future angle of the vector at instant $k + \Delta t$ could be estimated as $\theta(k + \Delta t) = \theta(k) + \omega\Delta t$. Hence, the grid voltage estimation can be computed as:

$$\boldsymbol{v}_g(k + \Delta t) = |\boldsymbol{v}_g|e^{j\theta(k+\Delta t)} = |\boldsymbol{v}_g|e^{j(\theta(k)+\omega\Delta t)} \tag{4.24}$$

4.1.9.2 Lagrange extrapolation

The vector angle compensation has the limitation that it can only be applied in variables that can be represented as a rotating vector. In the case of zero-sequence variables, this is not possible. Therefore, a possible solution is to calculate the one-step-ahead prediction using the nth-order formula of Lagrange extrapolation [57]:

$$\hat{\mathrm{x}}(k + 1) = \sum_{l=0}^{n}(-1)^{n-l}\begin{bmatrix} n+1 \\ l \end{bmatrix}\mathrm{x}(k + l - n) \tag{4.25}$$

where $\hat{x}$ could be the zero-sequence current reference $i_g^{\star\gamma}$ or grid-voltage v_g^{γ}. For sinusoidal variables the second order ($n = 2$) formula is sufficient for a good performance of the extrapolation (Eq. (4.26)) [56]. Despite of the aforementioned, the performance of this method decreases against step changes of the variables.

$$\hat{\mathbf{x}}(k + 1) = 3\mathbf{x}(k) - 3\mathbf{x}(k - 1) + \mathbf{x}(k - 2) \tag{4.26}$$

4.1.10 Overview of the proposed method

Providing an overview of the application of the proposed method will help the reader better understand its functioning. With this intention, a flowchart has been developed and presented in Fig. 4.6.

First, it is necessary to calculate the steady-state voltage $\boldsymbol{u}_{ss}(k)$ (equation (4.13)) and the deadbeat voltage $\boldsymbol{u}_{db}(k)$ (equation (4.12)) vectors in order to compute the unconstrained voltage vector $\boldsymbol{u}_{uc}(k)$ (equation (4.17)), which is the voltage to be synthesized by the converter. Then, the projection of $\boldsymbol{u}_{uc}(k)$ must be located within a region $\mathcal{S}_\ell$ of the hexagon in the $\alpha\beta$-plane, which is done by using equation (4.20). In this way, it is possible to obtain the four tetrahedrons $\mathcal{T}_j \in \mathcal{R}$ that will serve as candidates for the optimal solution.

Later on, the iteration begins among the four selected tetrahedrons to find the solution to the optimization problem. To achieve this, the equation (4.18) must be utilized in order to obtain the relaxed solution at each iteration. This process finds the local solution of each tetrahedron, hence a criterion is required to determine which of these four results corresponds to the global solution of the problem.

Under the assumption that $\boldsymbol{u}_{uc}(k)$ falls within the control region, i.e., $\boldsymbol{u}_{uc}(k) \in \mathcal{R}$, then there exists only one region $\mathcal{T}^\star$ able to generate $\boldsymbol{u}_{uc}(k)$ through a convex combination of its four switching vectors. In other words, only one among all the local solutions satisfies the constrain $d(k) \geq 0$; and hence, it will be the global optimal solution $d^\star$.

If none of the local solutions meet the non-negativity constraint $d(k) \geq 0$, it is concluded that $\boldsymbol{u}_{uc}(k)$ lies outside of the control region $\mathcal{R}$. Then, the duty cycles $\boldsymbol{d}_j$ and the value of the objective function J_j are computed by using equation (4.19) and (4.10), respectively, in every iteration. Finally, the solution yielding the smallest value of the objective function is selected, and the references that will be subsequently sent to the modulator are computed using the equation (4.22).

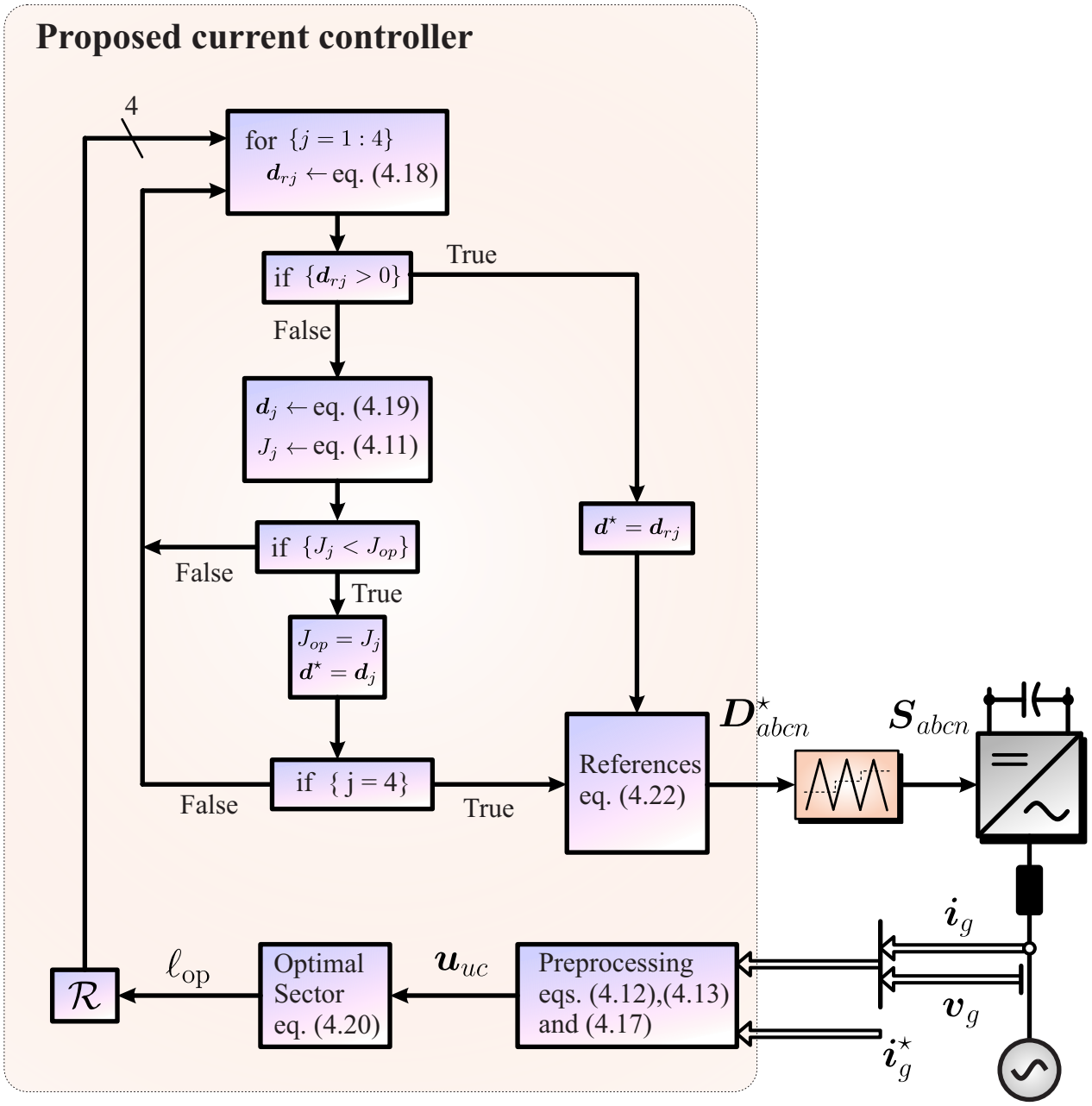

Figure 4.6: Flowchart of the proposed current control strategy.

Chapter 5

Simulation and Experimental results

5.1 Simulation results

Simulations of the 4L-2L converter connected to the grid through a RL-filter were carried out using the softwares MATLAB 2021b and PLECS Blockset 4.5.8. These simulations were performed in order to validate the experimental results shown in the following sections. Besides, comparisons with traditional PR controller are made to demonstrate the features of the controller proposed in this work. The system parameters are summarized in Table 5.1. For better visualization of the main variables, the grid variables were normalized with respect to their base quantities, i.e., $V_B = \sqrt{2/3}V_{\mathrm{R}}$, $I_B = \sqrt{2}I_{\mathrm{R}}$.

To demonstrate the performance of the proposed control scheme several simulations were implemented. In all of them, a switching frequency of 7.5 [kHz] and a pf = 1 were utilized. In Fig. 5.1a the system response to a step-change in $\alpha\beta\gamma$ current references is shown. It can be seen that the response of the system is fast and with good reference tracking in all control variables. The same simulation is performed twice changing the zero-sequence current reference with a sinusoidal reference of 250 [Hz] and a triangular reference, in Fig. 5.1b and Fig. 5.1c respectively.

Table 5.1: Parameters of the Experimental Setup phase and neutral inductance have a value of 10% and 5% of the base impedance, respectively.

Rated values		Param.	Value	Controller
I_{R}	$10/\sqrt{2}$ A	L_f	5.0 mH	$\lambda^{\alpha}_{u0} = \frac{V_{\mathrm{dc,R}}}{L_f}T_{\mathrm{p}}$
V_{R}	$110\sqrt{3}$ V	L_n	2.5 mH	$\lambda^{\alpha}_{u0} = \frac{V_{\mathrm{dc,R}}}{L_f}T_{\mathrm{p}}$
$V_{\mathrm{dc,R}}$	365 V	R_f	0.5 Ω	$\lambda^{\gamma}_{u0} = \frac{V_{\mathrm{dc,R}}}{L_\gamma}T_{\mathrm{p}}$

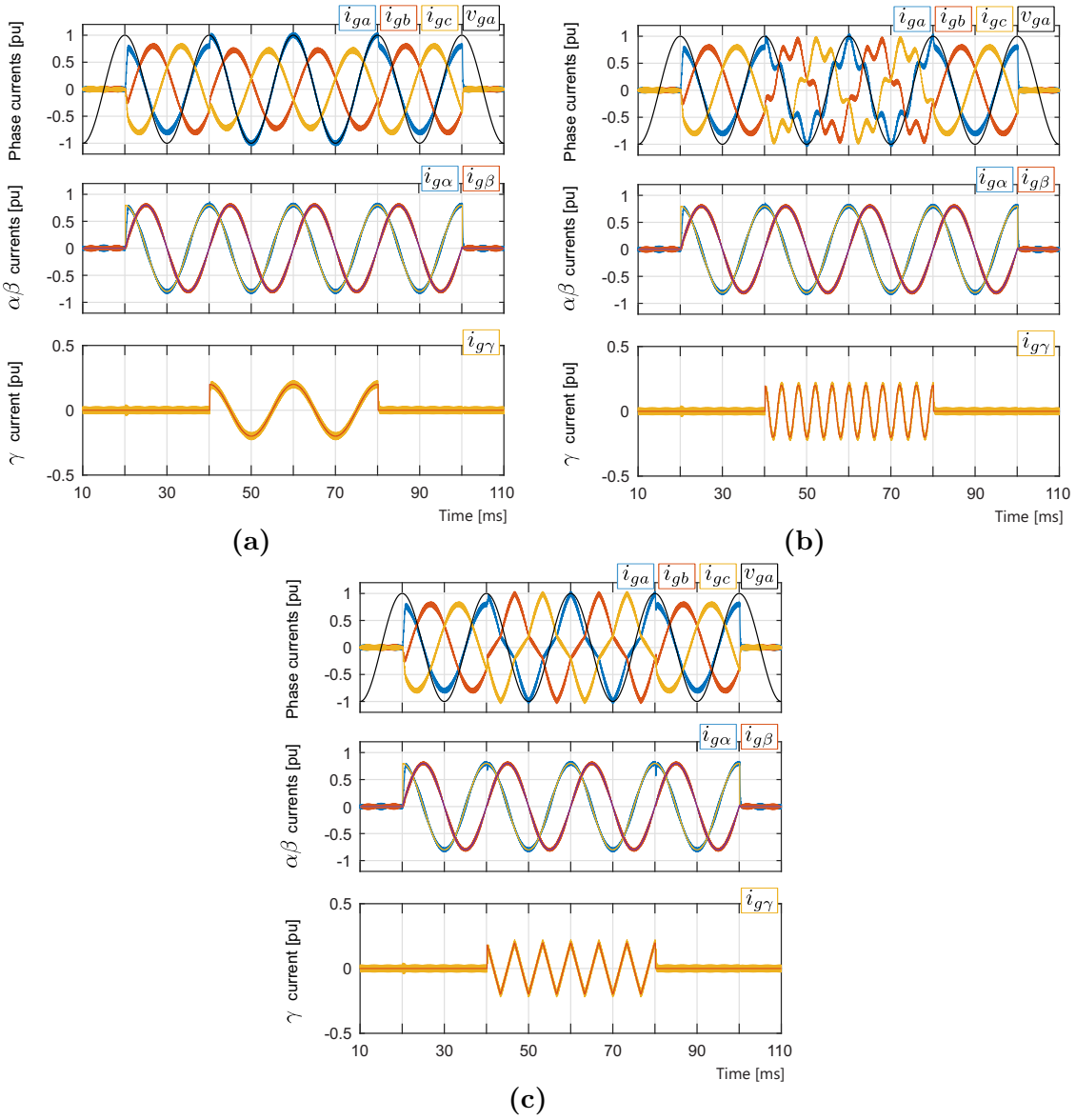

Figure 5.1: (a) Positive- and zero-sequence current step-changes, both at the fundamental frequency, (b) Zero-sequence current step-change of 250 Hz (c) sinusoidal and triangular references, respectively.

In these two tests is probed again that the proposed controller has a fast transient response and good reference tracking, regardless of the waveform of the reference current. It is worthily to highlight that all these tests were computed without changing any parameter of the controller, proving the versatility of the proposed MPC strategy.

The next simulations reveal the transient response of the proposed MPC scheme during a step change of the current reference. In Fig. 5.2a a whole fundamental cycle of the unconstrained voltage u_{uc} is displayed. Fig. 5.2b is a more detailed view of Fig. 5.2a. At an arbitrary instant of time the step response in current reference occurs

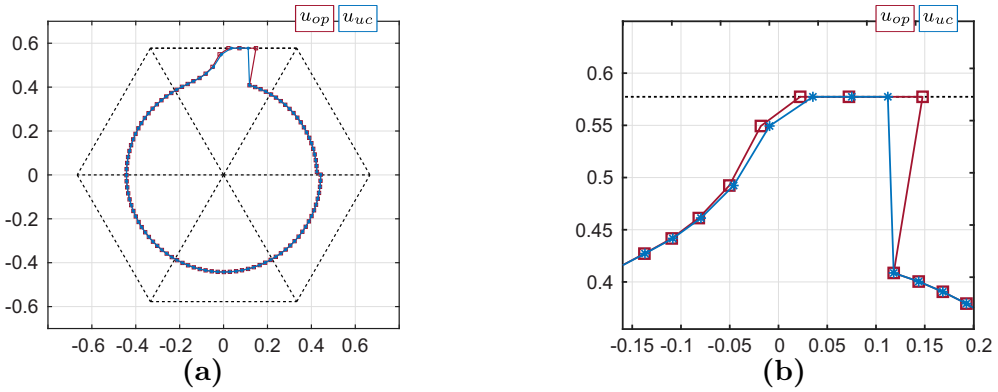

Figure 5.2: Transient response of the proposed MPC strategy. u_{op} is the optimal solution obtained with Matlab solver and u_{uc} corresponds to the solution obtained with proposed scheme showed in section 4.1.4. (a) u_{uc} response to step-change in $\alpha\beta$ current-references (b) Zoom of image in (a).

producing that the controller actuation saturates. This simulation was carried out twice, first with the proposed saturation scheme determined in the previous chapter (equation (4.19)), next, the test was repeated using the Matlab solver **lsqlin** to compare if the results obtained with the proposed saturation scheme was optimal. The results shown in Fig. 5.2 demonstrate that the method utilized is sub-optimal.

To conclude with the validation of the proposed method, a comparison is made with the traditional PR controller. In Fig. 5.3a and Fig. 5.3b, the response to step-change of current reference for both controllers is presented. It can be noticed that the the proposed MPC strategy has a faster dynamic response compared with traditional PR. This is due to the fact that the MPC strategy is able to take advantage of all the available actuation as it utilize the entire region of the hexagon generated by the states of the converter (Fig. 5.2a). In the 4L-2L converter the entire modulation region is the polyhedron shown in Fig. 3.5, the analysis is only made in $\alpha\beta$ plane to make the example easier, but the same idea can be extrapolated to the γ axis. In contrast with PR controller that it is only able to use the modulation region within the circumscribed circle in the hexagon.

Finally, to end this comparison, both controllers were tested against changes in the grid voltage. Fig. 5.4a presents the behaviour of the system under a step-change in $\alpha\beta$ voltage components of the grid. Again, the MPC strategy shows to be able to compensate this perturbation without even noticing an important change in the grid currents. Contrary to the PR controller, which shows a perturbation in the grid currents. This behaviour is also visible in Fig. 5.4b where the system is tested under unbalanced grid voltages with the presence of zero-sequence voltage.

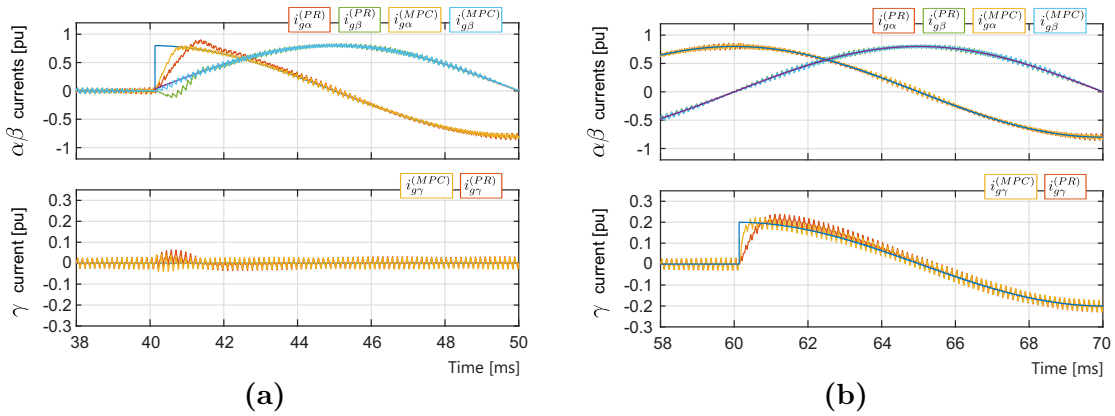

Figure 5.3: Comparison of the proposed MPC strategy and PR controller. (a) Step-change in $\alpha\beta$ currents and (b) Step-change in γ current.

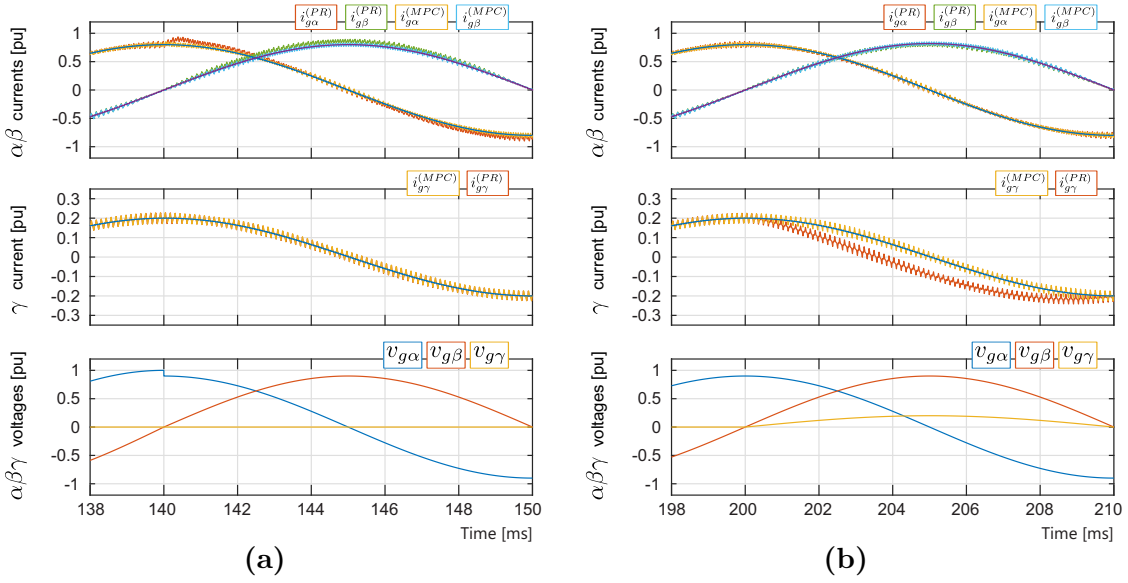

Figure 5.4: Comparison of the proposed MPC strategy and PR controller. (a) Step-change in $\alpha\beta$ grid-voltages and (b) Step-change in γ grid-voltage.

5.2 Experimental results

The performance of the proposed control strategy is evaluated in this section. To this end, the control algorithm was implemented in a DSP based on the Texas Instrument TMS320C6713 operating at 225 MHz platform augmented with a Xilinx FPGA Spartan 6-based board. The FPGA platform was programmed to handle the 12-bit analog-to-digital converters (ADC) and the carrier-based modulator to synthesize the desired OSS as explained in section 4.1.7. The laboratory setup shown in Fig. B.1 and Fig. B.2 (see Apendix B) was used for the purpose of this work. A diagram of this setup is displayed in Fig. 5.5. First, a six-pulse bridge rectifier for the DC-link is fed by three-phase variac connected to the grid through an isolation transformer. The converter's output is connected to the programmable power supply

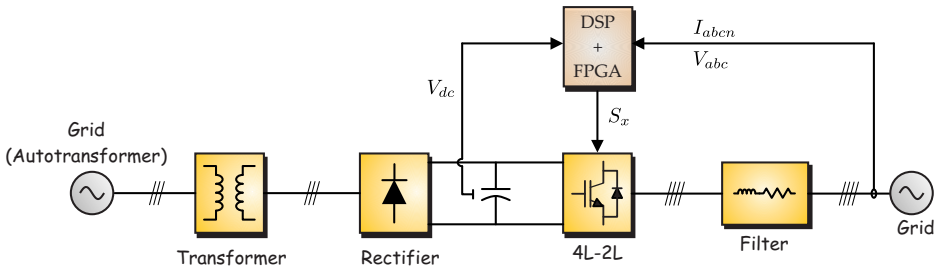

Figure 5.5: Laboratory setup diagram.

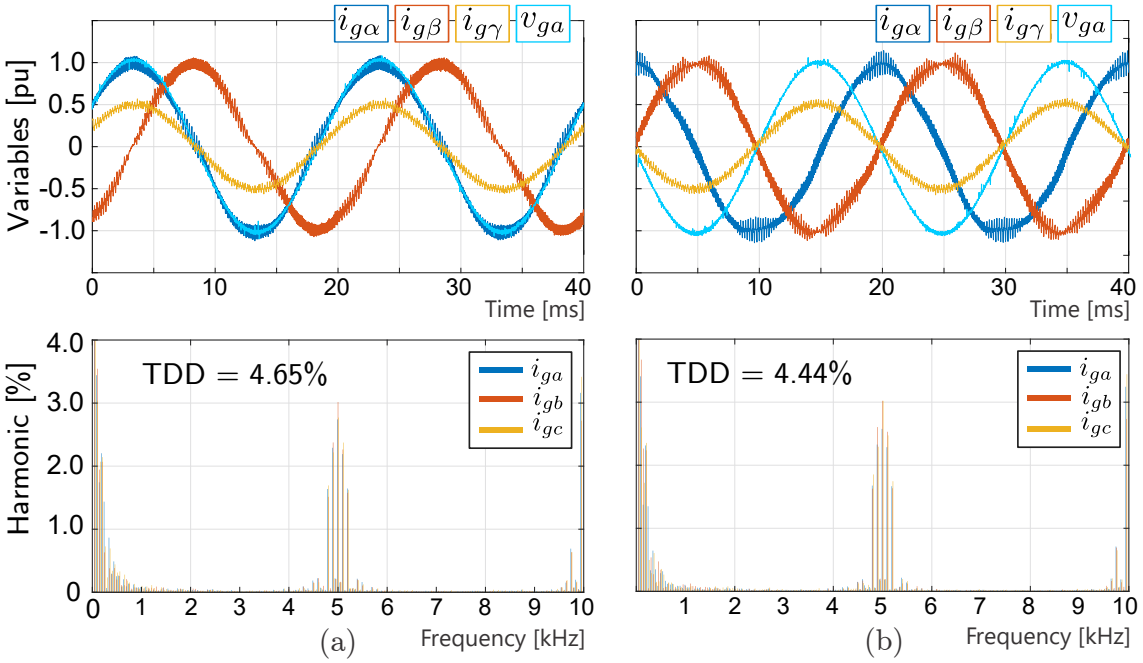

Figure 5.6: Steady-state performance at f_s=5 kHz: (a) PF=1; (b) PF = 0.

(Ametek, model MX45) through an inductive filter that emulates the grid. An IRG4PH40UD IGBT was used in the converter prototype.

Experimental tests include steady-state and dynamic conditions for the grid-connected configuration. The system parameters are the same used in the simulations which were summarized in Table 5.1. Analogously to how it was done in the simulation section the grid variables were normalized with respect to their base quantities, i.e., V_B, I_B.

5.2.1 Steady-State Performance

To evaluate the performance of the system, the TDD from equation (3.1) is utilized. The steady-state performance of the grid currents in the $\alpha\beta\gamma$ framework is shown in Fig. 5.6. The switching frequency of the converter is set as $f_s = 5$ kHz. The amplitude references of the $\alpha\beta$ components are the rated current (namely, $I^{\alpha}_{g,\text{ref}} = I^{\beta}_{g,\text{ref}} = 10$ A), and the γ-component is $I^{\gamma}_{g,\text{ref}} = 5$ A. Fig. 5.6(a) shows

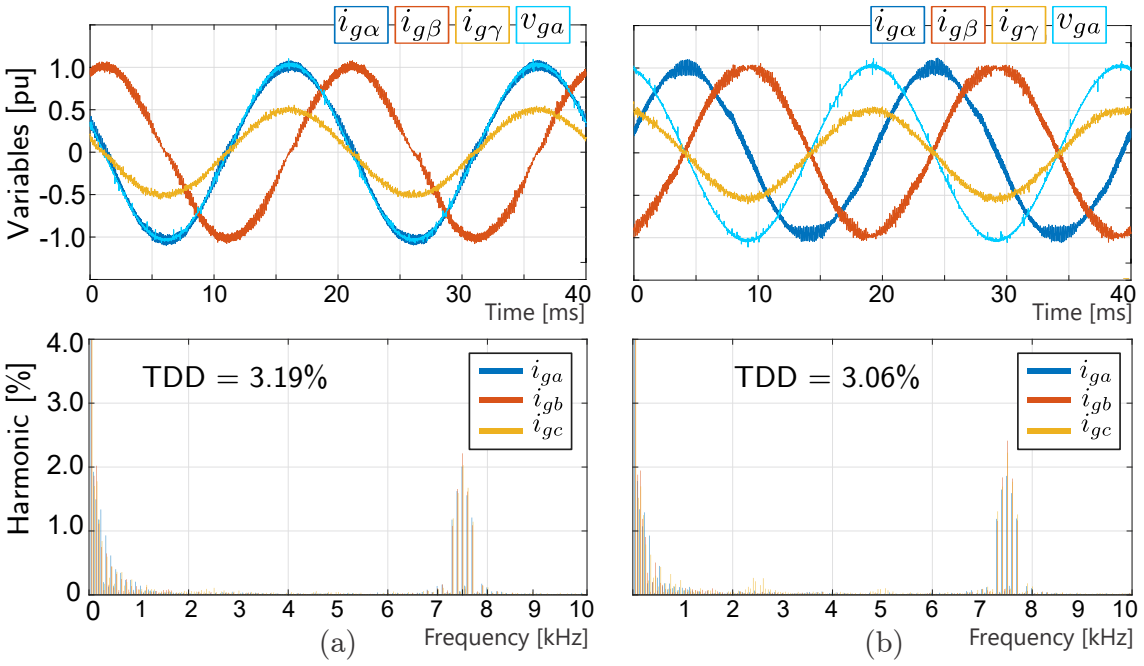

Figure 5.7: Steady-state performance at f_s=7.5 kHz: (a) PF =1; (b) PF = 0.

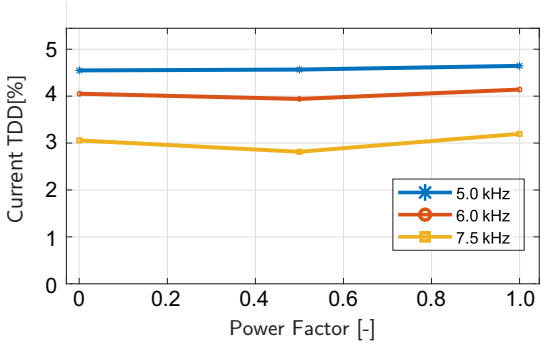

Figure 5.8: Experimental current TDD at rated power as function of the power factor for three switching frequencies.

the experimental waveforms operating with unity power factor (PF), meanwhile Fig. 5.6(b) is with PF = 0, injecting rated reactive power to the grid. For both cases, the injected current in the neutral is in phase to the neutral-to-line voltage v_{ga}. Besides, as observed in the second row of Fig. 5.6, the proposed MPC strategy imposes a shaped harmonic spectrum in which the amplitude of all harmonic components of the three-phase currents are below 3%, achieving, accordingly, a low TDD for both cases (on average 4.65% and 4.44%, respectively). Also, as depicted in these harmonic spectra, the high-frequency harmonic components are concentrated at 5 kHz, which corresponds to the carrier-signal frequency.

Fig. 5.7 shows the same steady-state performance validation as in Fig. 5.6, but using a higher switching frequency f_s = 7.5 kHz. As seen, the experimental results are similar since the amplitudes of the $\alpha\beta\gamma$-components are tracking the desired values. Still, the high-frequency harmonic components and the side-bands are

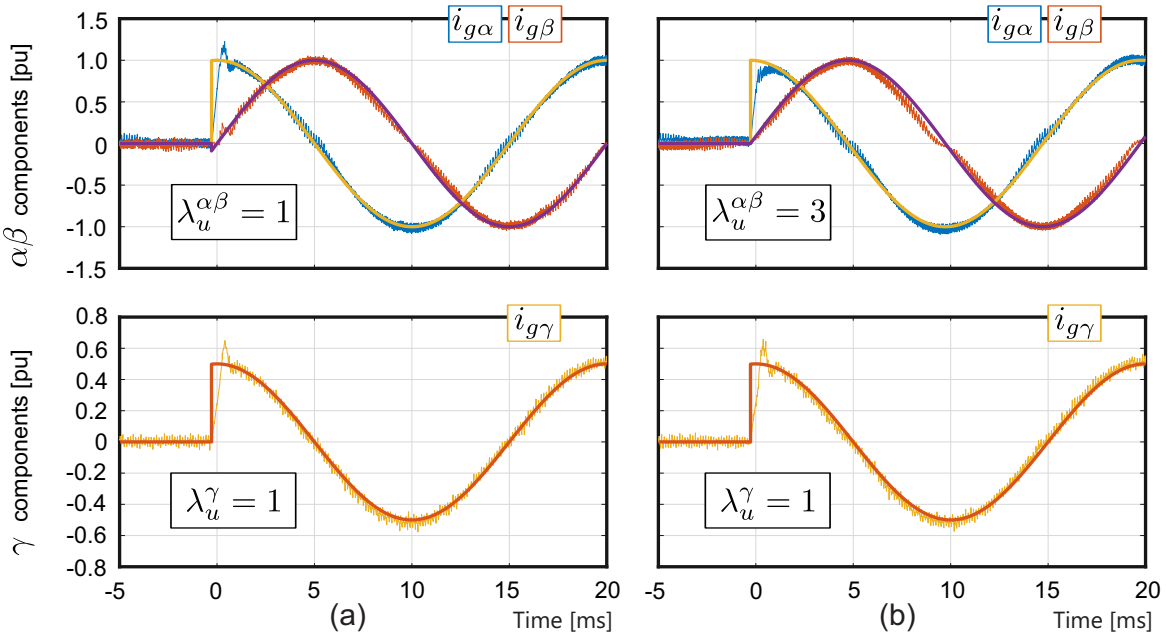

Figure 5.9: Effect of the tuning parameter $\lambda_u^{\alpha\beta}$ on the transient performance while keeping λ_u^{γ} constant: sinusoidal references.

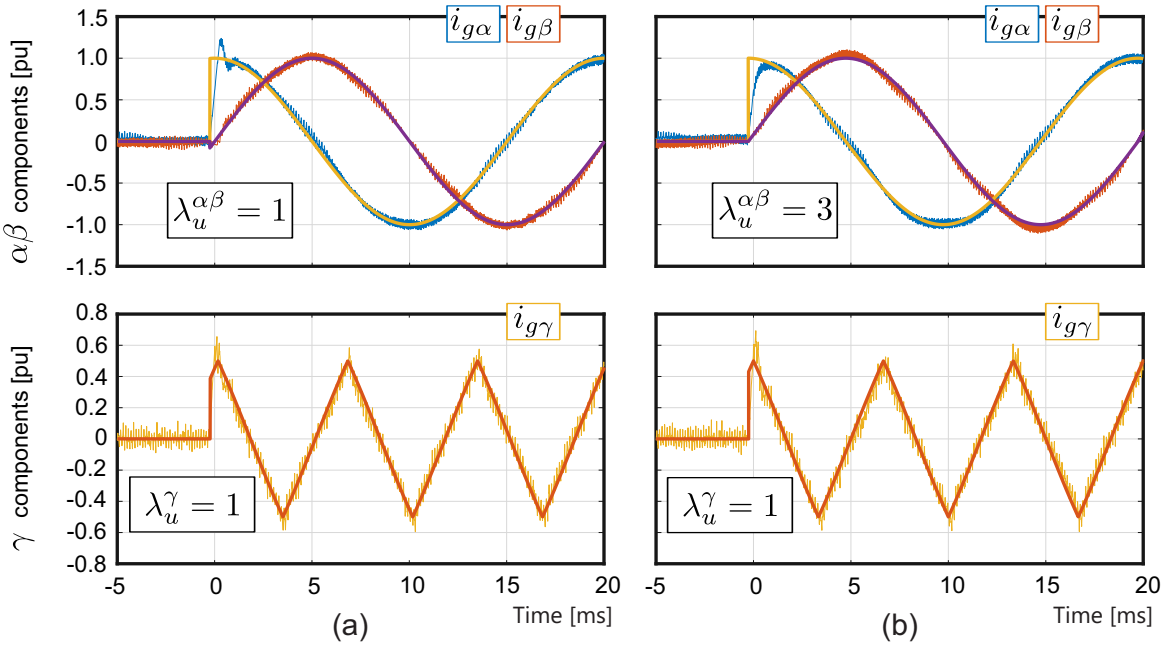

Figure 5.10: Effect of the tuning parameter $\lambda_u^{\alpha\beta}$ on the transient performance while keeping λ_u^{γ} constant: triangular reference for current i_g^{γ}.

centered at 7.5 kHz; meanwhile, the current TDD is reduced in the same proportion as the switching frequency increases (on average 3.19% and 3.06%, respectively). Additionally, Fig. 5.8 resumes the average value of the current TDD at rated current for different switching frequencies and power factors.

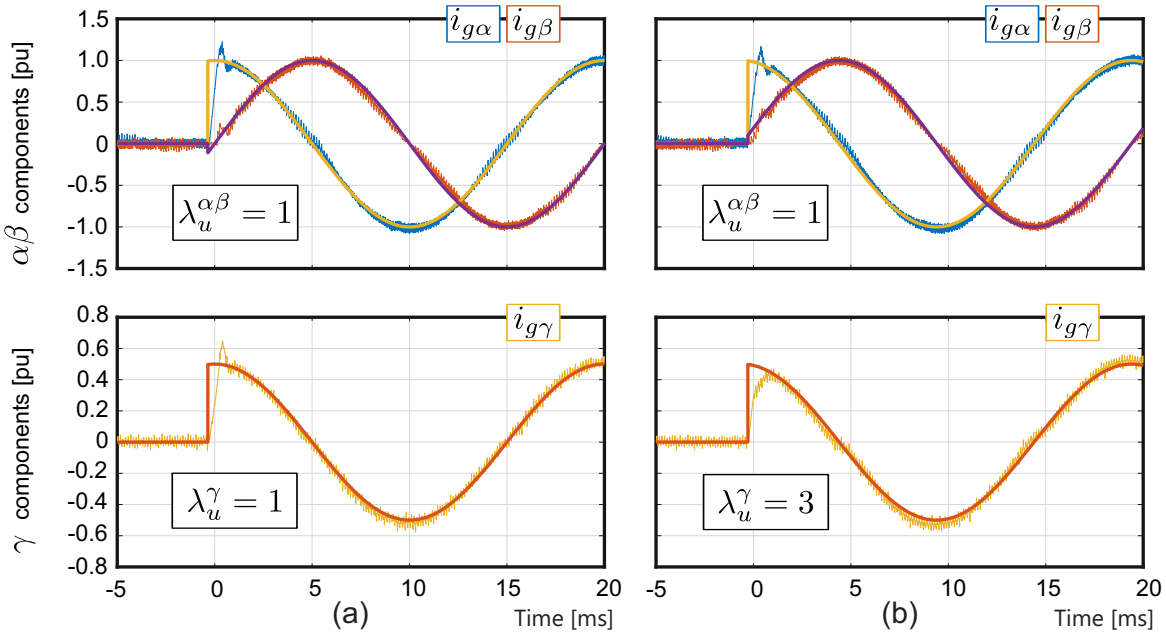

Figure 5.11: Effect of the tuning parameter λ_u^{γ} on the transient performance while keeping $\lambda_u^{\alpha\beta}$ constant: sinusoidal references.

5.2.2 Effect of the Tuning Parameters.

In this section, four experiments were performed to demonstrate the effect of the tuning matrix $\mathbf{\Lambda}_u = \text{diag}(\lambda_u^{\alpha}, \lambda_u^{\beta}, \lambda_u^{\gamma})$ on the dynamic performance of the controlled system. The switching frequency of the converter is set as 7.5 kHz. For all studied cases, sinusoidal references with rated amplitude are imposed for the $\alpha\beta$ components, i.e., $I_{g,\text{ref}}^{\alpha\beta} = 10$ A. In addition, the γ-component performance is evaluated under two signal references: a sinusoidal of fundamental frequency, and a triangular of 150 Hz with peak values of 5 A.

5.2.2.1 Tuning parameter $\lambda_u^{\alpha\beta}$

Fig. 5.9 and Fig. 5.10 compare the dynamic response of the grid currents for two different tuning parameters $\lambda_u^{\alpha\beta}$ when a step-change at instant $t = 0$ is applied. As shown in these graphics, a lower value of $\lambda_u^{\alpha\beta}$ produces a more aggressive dynamic response with a slight overshoot during transients. Besides, the change of $\lambda_u^{\alpha\beta}$ does not impact on the transient response of current i_g^{γ}. This decoupled behavior is observed for the sinusoidal and triangular reference.

5.2.2.2 Tuning parameter λ_u^{γ}

Analogously, Fig. 5.11 and Fig. 5.12 compare the dynamic response of the grid currents for two different tuning parameters λ_u^{γ}. As shown in these graphics, a lower value of λ_u^{γ} produces a more aggressive dynamic response but a better tracking of the triangular signal reference (see Fig. 5.12). Moreover, the experimental results depicted in these figures show exactly the same dynamic response for the $\alpha\beta$ components regardless of the value of λ_u^{γ} and the reference signal of current i_g^{γ}, demonstrating

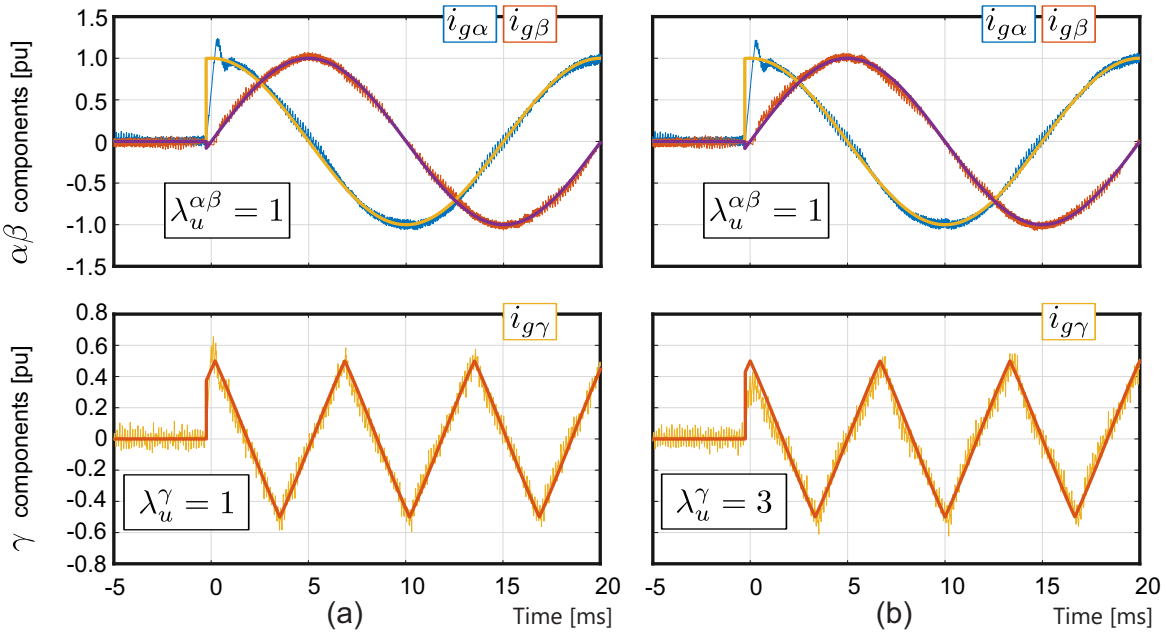

Figure 5.12: Effect of the tuning parameter λ_u^{γ} on the transient performance while keeping $\lambda_u^{\alpha\beta}$ constant: triangular reference for current i_g^{γ}.

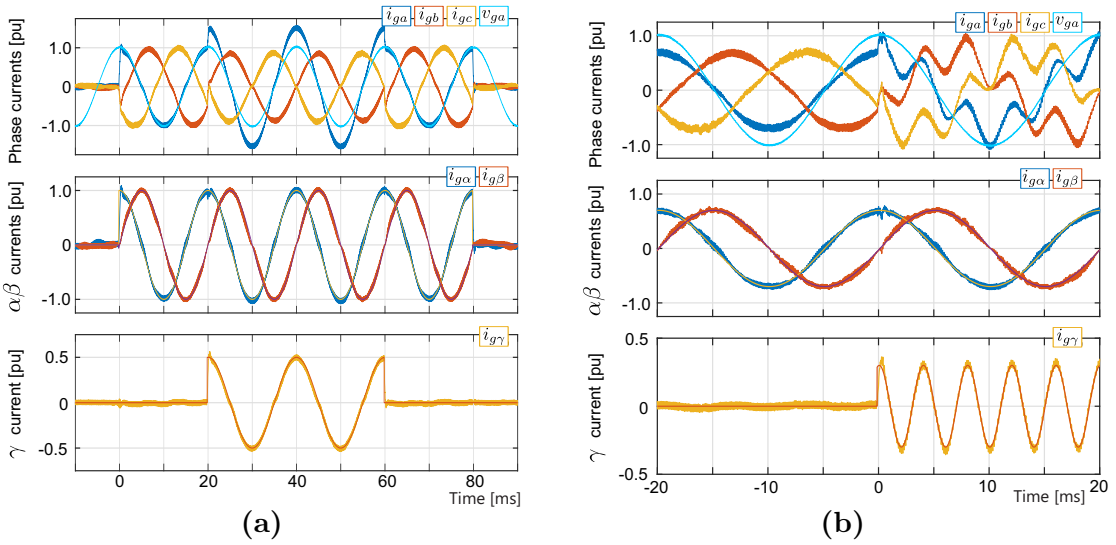

Figure 5.13: (a) Positive- and zero-sequence current step-changes, both at the fundamental frequency and (b) Zero-sequence current step-change of 250 Hz.

that the dynamic response of the $\alpha\beta$ components of the grid currents can be set in a decoupled manner of the γ component.

Notice the good tracking performance of the triangular waveform reference achieved in this subsection. These waveforms are not simple to track using conventional PI and PR controllers.

5.2.3 Dynamic Performance.

Finally, two tests were performed to demonstrate adequate reference tracking in the presence of two different frequencies for the neutral current: 50 and 250 Hz. On the one hand, the behavior of the grid current is shown in Fig. 5.13a when reference step changes are imposed at different instants for the $\alpha\beta$ and γ components. Firstly, a rated positive-sequence current is injected at instant 0 seconds, and then, at instant 0.2 seconds, a zero-sequence current reference of amplitude 0.5 pu is included. On the other hand, the second test (Fig. 5.13b) demonstrates good tracking in the presence of a current in the neutral with a frequency equal to five times the fundamental. In both cases, a slight coupling between $\alpha\beta$ and γ current components arises when step-changes are applied in the command signals.

5.2.4 Execution time of the proposed control strategy

A test to measure execution time of the proposed algorithm was performed. To do this a LED included in the DSP board was used. The idea was to turn on the LED before the algorithm was executed, and after the algorithm reaches its end an instruction to turn off the LED was sent. The oscilloscope Keysight InfiniiVision DSOX3014T of 5 GSa/s was used to measure the time that the LED remained turned on.

Results shown in Fig. 5.14 illustrates the execution time for the proposed algorithm explained in section 4.1.5 that allows to solve the optimal problem by iterating only on 4 of the 24 tetrahedra that constitutes the control region. On the contrary, Fig. 5.15 shows the execution time of the algorithm that solves the sub-optimal problem for all of the 24 tetrahedra. The test results demonstrates that the proposed algorithm solves the optimal problem in less than a third of the time required by the exhaustive method, 83 μs and 295 μs, respectively.

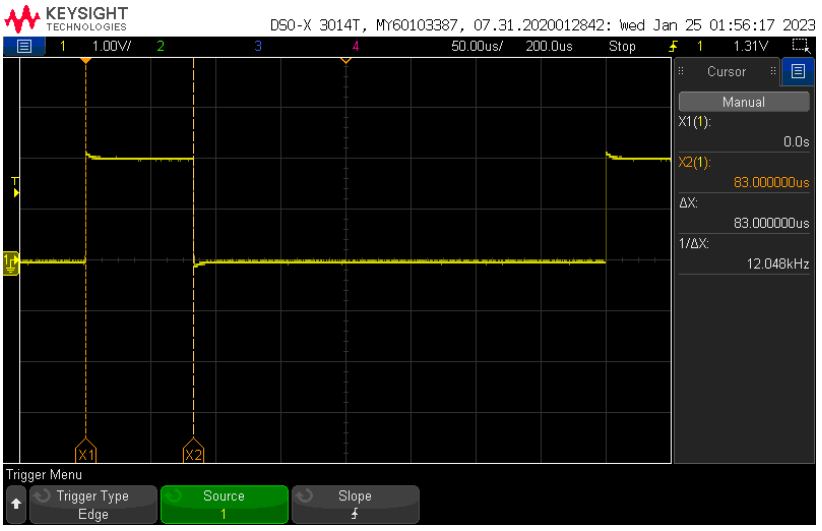

Figure 5.14: Execution time of the proposed control strategy.

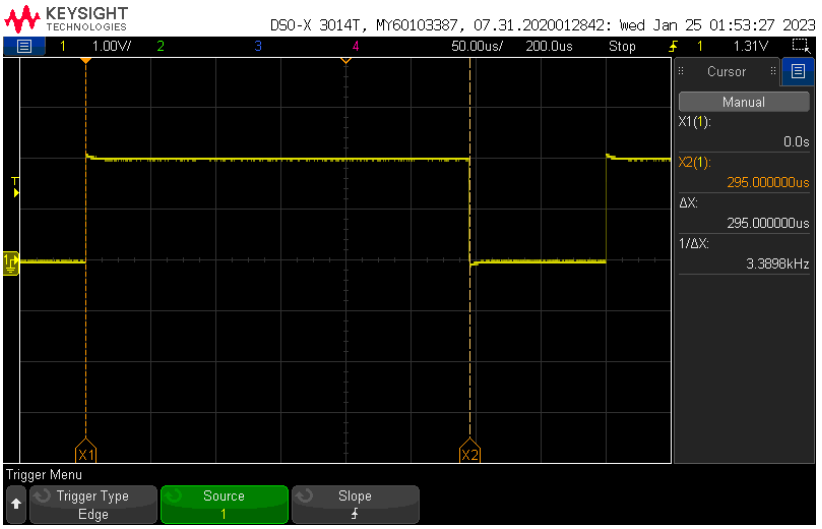

Figure 5.15: Computational.

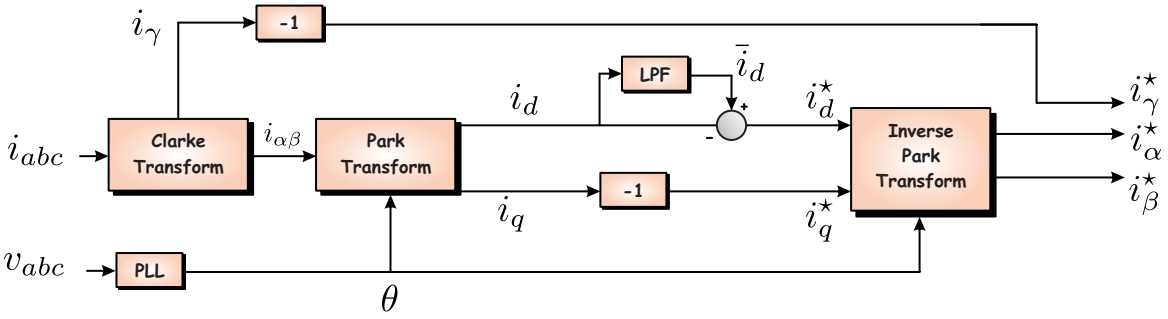

Figure 5.16: Reference generator used in this work to obtain the current reference for the controller. LPF = Low Pass Filter and PLL = Phase-Locked Loop. Current references are: $i_d^\star = -\tilde{i}_d$ and $i_q^\star = -\left(\bar{i}_q + \tilde{i}_q\right)$, where the variables $\tilde{i}$ and $\bar{i}$ are the sinusoidal and average component of the current.

5.2.5 Assessment as a Shunt Active Filter

This section presents the performance of a 4L-2L Shunt Active Filter (4L-SAF) governed by the proposed current controller. The current reference generator introduced in [12] and shown in 5.16 is implemented in these experiments to calculate the reference signal currents required by the converter to compensate for reactive power, current harmonic, and current imbalance. To this end, a nonlinear load based on a six-pulse rectifier feeding an RC load is used, as illustrated in the unilineal diagram of Fig. 5.17. In addition, an unbalanced RL load connected in parallel is used to produce a current imbalance. In this case, the converter's switching frequency is set as 5.0 kHz.

The experimental validation of the proposed controller governing a shunt active filter is presented in Fig. 5.18. As shown in Fig. 5.18(a)-(b), previously to instant $t = 0$ seconds, the current delivered by the source i_{sa} contains harmonics and is unbalanced since the neutral current i_{sn} is not equal to zero. In $t = 0$, the 4L-SAF

is turned on, and the current injected by the filter [see waveform in Fig. 5.18(c)] allows compensating for the current harmonics and the reactive power. Moreover, Fig. 5.18(b) shows that the system neutral current is effectively compensated and eliminated. The measured displacement power factor (DPF) is 0.997, and the power factor is 0.976.

Furthermore, to compare the performance of the proposed controller with some conventional methods, the shunt active filter operation presented in Fig. 2.2 was performed using the standard FCS-MPC strategy presented in [12]. The control algorithm calculates the 16 cost function values associated with the set of possible switching vectors and selects the one with the minimal cost function. Unfortunately, due to the computational burden of this control strategy (the measured execution time is 53 μs), the sampling frequency could not be increased over 15 kHz with the low-cost control platform utilized in the converter prototype. Consequently, an average switching frequency of 3.025 kHz is obtained.

Fig. 5.19 shows the dynamic behaviour obtained with the FCS-MPC strategy considering the same transient test presented in Fig. 5.18. By visual inspection, it is clear that the proposed control strategy outperforms the standard FCS-MPC approach. During steady-state, the measured DPF is 0.987, and the power factor is 0.929. Although this comparison is somehow unfair since the (average) switching frequencies are not equal, the comparison is made considering the best possible performance of the FCS-MPC that can be obtained using the low-cost control platform utilized in the converter prototype. Therefore, to get similar performances, the FCS-MPC approach should be implemented in a more powerful control card, which certainly increases the cost of the overall converter.

5.2.6 Impact of the Parameters Mismatch

Finally, to evaluate the influence of model parametric uncertainties on the performance of the proposed predictive strategy, we will analyze the $\alpha\beta$ components separately of the γ component. In this regard, the parameter mismatches are modeled as $\hat{L}_f{=}\mu_L L_f$ and $\hat{R}_f{=}\mu_R R_f$. Under this perspective, it is straightforward to demonstrate that the deadbeat voltage error, defined as $\Delta\boldsymbol{v}_{\rm db}{=}V_{\rm dc}(\boldsymbol{u}_{\rm db}{-}\hat{\boldsymbol{u}}_{\rm db})$, can be expressed as:

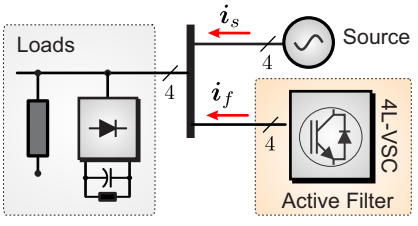

Figure 5.17: Unilineal diagram of the experimental setup used for testing the shunt active filter.

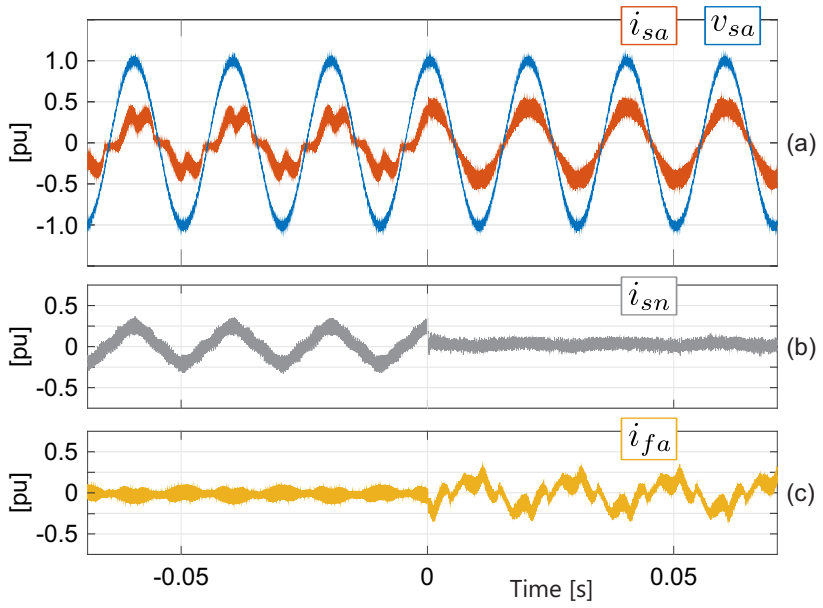

Figure 5.18: Shunt active filter operation at f_s=5 kHz: (a) source voltage v_{sa} and current i_{sa}; (b) converter current i_{fa} (filter current); and (c) source neutral current i_{sn}.

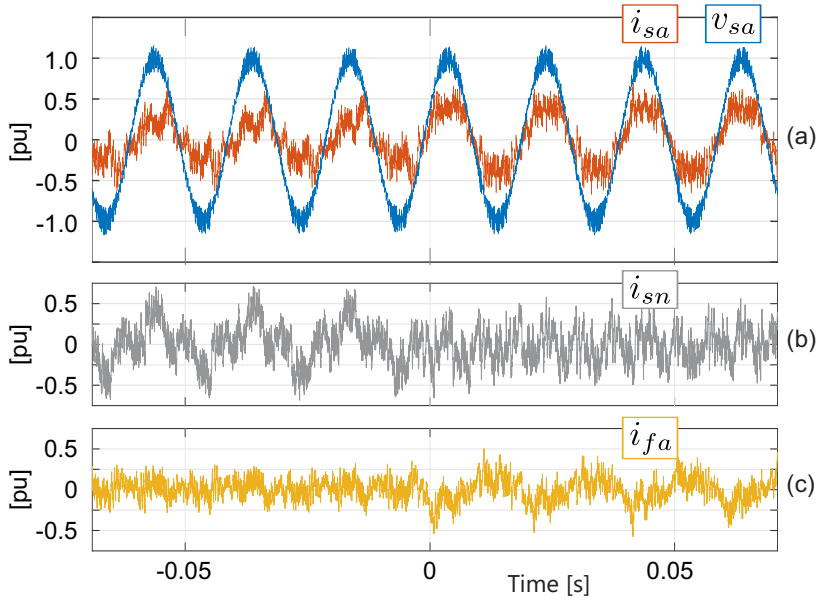

Figure 5.19: FCS-MPC performance: (a) v_{sa} and i_{sa}; (b) i_{fa}; and (c) i_{sn}.

$$\begin{aligned}\Delta \boldsymbol{v}_{\mathrm{db}}^{\alpha\beta} =& \frac{L_f}{T_p}(1-\mu_L)\left(\boldsymbol{i}_{\mathrm{g,ref}}^{\alpha\beta}(k+1) - \boldsymbol{i}_{\mathrm{g}}^{\alpha\beta}(k)\right) \\ &+ R_f(1-\mu_R)\,\boldsymbol{i}_{\mathrm{g}}^{\alpha\beta}(k)\end{aligned} \tag{5.1}$$

As shown in (5.1), the deadbeat voltage error is not only determined by the parameters mismatch but also by the instantaneous values of the tracking error and the grid

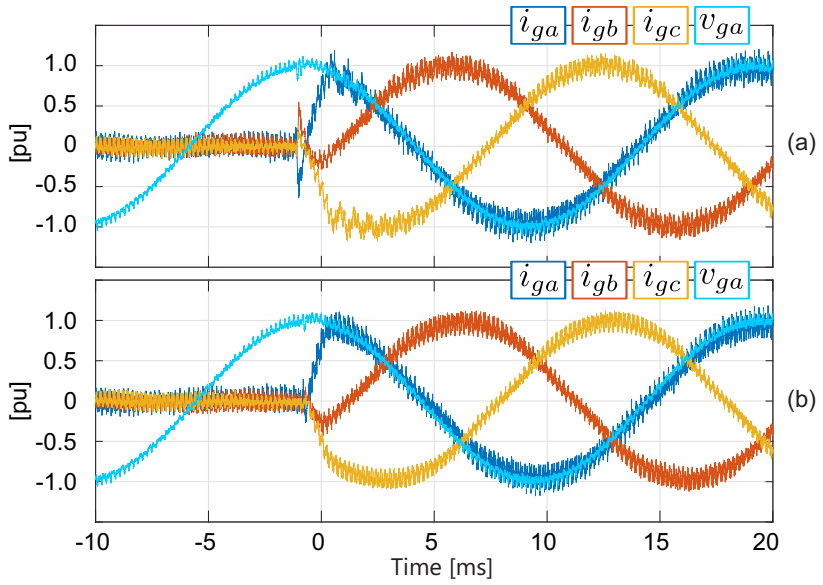

Figure 5.20: Effect of parameter mismatch on the controller system performance: (a) overestimated inductance $\mu_L = 1.5$; and (b) underestimated inductance $\mu_L = 0.5$. Switching frequency 5 kHz.

current vector. Thereby, $\Delta \boldsymbol{v}_{\mathrm{db}}^{\alpha\beta}$ is very susceptible to inductance mismatches $\mu_L \neq 1$ during transient operation in which the tracking error, i.e., $\boldsymbol{e}(k) = \boldsymbol{i}_{\mathrm{g,ref}}^{\alpha\beta}(k{+}1) - \boldsymbol{i}_{\mathrm{g}}^{\alpha\beta}(k)$ becomes predominant. However, during steady-state, the effect of μ_L is mitigated since the tracking error is reduced. On the other hand, a resistance discrepancy $\mu_R \neq 1$ does not significantly affect the deadbeat voltage error because the resistance is minimised during the design of the output filter, i.e., $L_f \gg T_{\mathrm{p}} R_f$.

Fig. 5.20 shows the transient response for one of the worse case conditions (where the reference current $\boldsymbol{i}_{\mathrm{g,ref}}^{\alpha\beta}(k)$ suddenly changes from zero to its rated amplitude) when an over- and under-estimated inductance value is used in the control algorithm. The steady-state tracking errors after the step change are 1.84% and 3.48%, for $\mu_L = 1.5$ and $\mu_L = 0.5$, respectively. Furthermore, the transient response of the proposed controller under filter resistance mismatches is depicted in Fig. 5.21. In this case, the tracking errors are 1.62% and 1.44%. Comparing the transient responses depicted in Fig. 5.20 and Fig. 5.21, it is evident that the controller is more affected by discrepancies in the inductance parameter than the resistance. These experimental results confirm the conclusions derived from (5.1) since the effect of the parameter mismatch on the closed-loop performance is more prominent during transients and more affected by discrepancies in the inductance parameter than the resistance.

Analogously, the effect of mismatch on the zero-sequence parameters, modeled as $\hat{L}_\gamma{=}\mu_{L\gamma} L_\gamma$ and $\hat{R}_\gamma{=}\mu_{R\gamma} R_\gamma$, is the same as the presented above for the $\alpha\beta$ components since the deadbeat voltage error for the γ component is given by:

$$\Delta v_{\mathrm{db}}^{\gamma}{=}\frac{L_\gamma}{T_{\mathrm{p}}}(1-\mu_{L\gamma})\left(i_{\mathrm{g,ref}}^{\gamma}(k{+}1) - i_{\mathrm{g}}^{\gamma}(k)\right) + R_\gamma(1-\mu_{R\gamma})\, i_{\mathrm{g}}^{\gamma}(k) \tag{5.2}$$

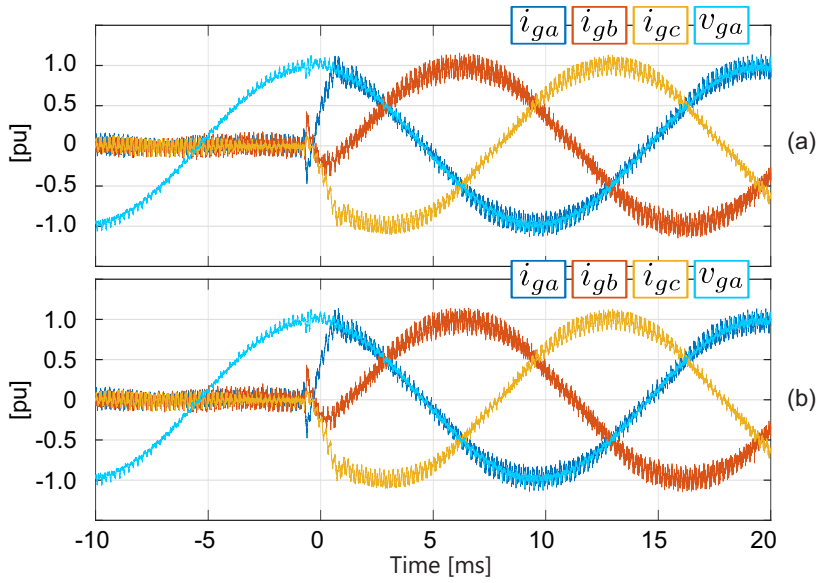

Figure 5.21: Effect of parameter mismatch on the controller system performance: (a) overestimated resistance $\mu_R = 1.5$; and (b) underestimated resistance $\mu_R = 0.5$. Switching frequency 5 kHz.

Therefore, zero-sequence parameter discrepancies would deteriorate more the transient responses than the steady-state performance.

Chapter 6

Conclusions

In this work, a MPC strategy based on optimal switching sequences is proposed for 4-leg grid-tied converters. Extensive experimental tests presented here have demonstrated that the proposed control method achieves a good performance in both steady-state and transient conditions, even for reference currents having high harmonic content.

The proposed OSS-MPC controller imposes the converter to operate with a fixed switching frequency and a predefined harmonic spectrum without compromising the inherent fast dynamic response of the predictive control strategies, showing the advantages of this method against traditional control strategies like PR and traditional OSS-MPC controllers. In addition, users can tune the controller in a decoupled manner to establish different dynamic responses on the α, β, and γ components of the grid-currents.

The novelty of this proposal lies in that the control algorithm efficiently determines the optimal tetrahedron and the application times of its switching vectors to provide the optimal switching sequence with a reduced computational burden. Consequently, the resulting MPC strategy can be implemented in low-cost control platforms without degrading dynamic or steady-state performance.

The optimal control problem underlying the proposed controller allows a straightforward and robust tuning of the OSS-based current controller. Consequently, no complex controller tuning is required to perform well for shunt active filter applications, as evidenced by the experimental assessment. Therefore, the proposed controller is suitable for three-phase four-wire shunt active filters.

Appendices

Chapter A

Table of tetrahedra and Switching Sequence

Table A.1: Tretrahedrons gruped by sectors.

Sector	Tetrahedron	Active vectors	Switching Sequence				
			$u_{s_{0N}}$	u_{s_x}	u_{s_y}	u_{s_z}	$u_{s_{0P}}$
S1	$\mathcal{R}_1$	u_1 u_9 u_{13}	0	0	1	1	1
			0	0	0	1	1
			0	0	0	0	1
			0	1	1	1	1
	$\mathcal{R}_2$	u_8 u_9 u_{13}	0	1	1	1	1
			0	0	0	1	1
			0	0	0	0	1
			0	0	1	1	1
	$\mathcal{R}_3$	u_8 u_{12} u_{13}	0	1	1	1	1
			0	0	1	1	1
			0	0	0	0	1
			0	0	0	1	1
	$\mathcal{R}_4$	u_8 u_{12} u_{14}	0	1	1	1	1
			0	0	1	1	1
			0	0	0	1	1
			0	0	0	0	1
S2	$\mathcal{R}_5$	u_1 u_5 u_{13}	0	0	0	1	1
			0	0	1	1	1
			0	0	0	0	1
			0	1	1	1	1
	$\mathcal{R}_6$	u_4 u_5 u_{13}	0	0	0	1	1
			0	1	1	1	1
			0	0	0	0	1
			0	0	1	1	1
	$\mathcal{R}_7$	u_4 u_{12} u_{13}	0	0	1	1	1
			0	1	1	1	1
			0	0	0	0	1
			0	0	0	1	1
	$\mathcal{R}_8$	u_4 u_{12} u_{14}	0	0	1	1	1
			0	1	1	1	1
			0	0	0	1	1
			0	0	0	0	1

Continuance of previous table

Sector	Tetrahedron	Active vectors	Switching Sequence				
			$u_{s_{0N}}$	u_{s_x}	u_{s_y}	u_{s_z}	$u_{s_{0P}}$
S3	$\mathcal{R}_9$	u_1 u_5 u_7	0	0	0	0	1
			0	0	1	1	1
			0	0	0	1	1
			0	1	1	1	1
	$\mathcal{R}_{10}$	u_4 u_5 u_7	0	0	0	0	1
			0	0	1	1	1
			0	1	0	1	1
			0	0	1	1	1
	$\mathcal{R}_{11}$	u_4 u_6 u_7	0	0	0	0	1
			0	1	1	1	1
			0	0	1	1	1
			0	0	0	1	1
	$\mathcal{R}_{12}$	u_4 u_6 u_{14}	0	0	0	1	1
			0	1	1	1	1
			0	0	1	1	1
			0	0	0	0	1
S4	$\mathcal{R}_{13}$	u_1 u_3 u_7	0	0	0	0	1
			0	0	0	1	1
			0	0	1	1	1
			0	1	1	1	1
	$\mathcal{R}_{14}$	u_2 u_3 u_7	0	0	0	0	1
			0	0	0	1	1
			0	1	1	1	1
			0	0	1	1	1
	$\mathcal{R}_{15}$	u_2 u_6 u_7	0	0	0	0	1
			0	0	1	1	1
			0	1	1	1	1
			0	0	0	1	1
	$\mathcal{R}_{16}$	u_2 u_6 u_{14}	0	0	0	1	1
			0	0	1	1	1
			0	1	1	1	1
			0	0	0	0	1

Continuance of previous table

Sector	Tetrahedron	Active vectors	Switching Sequence				
			$u_{s_{0N}}$	u_{s_x}	u_{s_y}	u_{s_z}	$u_{s_{0P}}$
S5	$\mathcal{R}_{17}$	u_1 u_3 u_{11}	0	0	0	1	1
			0	0	0	0	1
			0	0	1	1	1
			0	1	1	1	1
	$\mathcal{R}_{18}$	u_2 u_3 u_{11}	0	0	0	1	1
			0	0	0	0	1
			0	1	1	1	1
			0	0	1	1	1
	$\mathcal{R}_{19}$	u_2 u_{10} u_{11}	0	0	1	1	1
			0	0	0	0	1
			0	1	1	1	1
			0	0	0	1	1
	$\mathcal{R}_{20}$	u_2 u_{10} u_{14}	0	0	1	1	1
			0	0	0	1	1
			0	1	1	1	1
			0	0	0	0	1
S6	$\mathcal{R}_{21}$	u_1 u_9 u_{11}	0	0	1	1	1
			0	0	0	0	1
			0	0	0	1	1
			0	1	1	1	1
	$\mathcal{R}_{22}$	u_8 u_9 u_{11}	0	1	1	1	1
			0	0	0	0	1
			0	0	0	1	1
			0	0	1	1	1
	$\mathcal{R}_{23}$	u_8 u_{10} u_{11}	0	1	1	1	1
			0	0	0	0	1
			0	0	1	1	1
			0	0	0	1	1
	$\mathcal{R}_{24}$	u_8 u_{10} u_{14}	0	1	1	1	1
			0	0	0	1	1
			0	0	1	1	1
			0	0	0	0	1

Chapter B

Images of Laboratory Setup

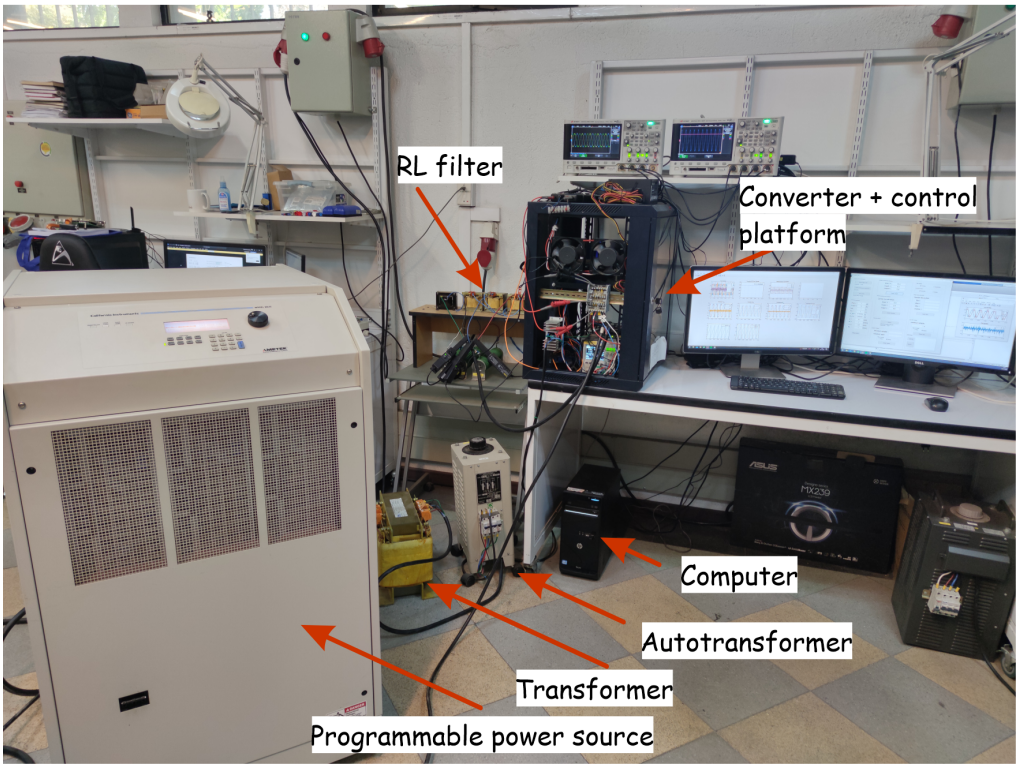

Figure B.1: Laboratory setup used for empirical results.

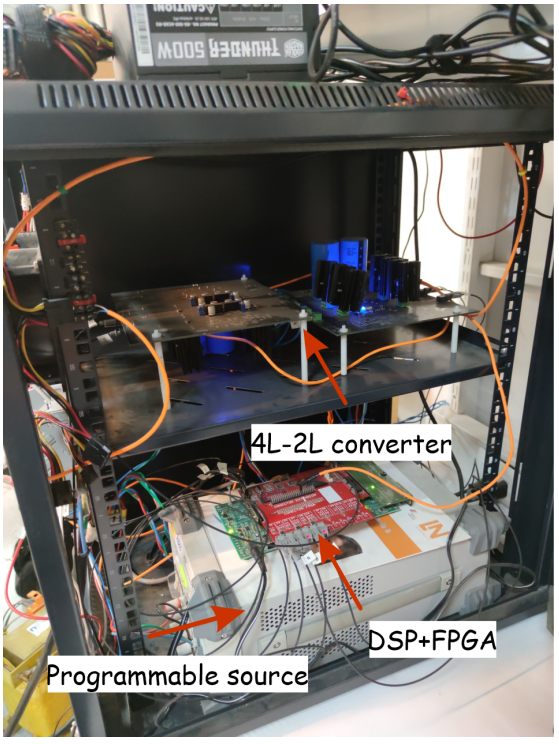

Figure B.2: Inside of the rack used to store the converter and control platform.

Bibliography

[1] S. Vazquez, J. Rodriguez, M. Rivera, L. G. Franquelo, and M. Norambuena, "Model Predictive Control for Power Converters and Drives: Advances and Trends," *IEEE Transactions on Industrial Electronics*, vol. 64, no. 2, pp. 935–947, 2017.

[2] "IEEE Recommended Practice and Requirements for Harmonic Control in Electric Power Systems," *IEEE Std 519-2014 (Revision of IEEE Std 519-1992)*, pp. 1–29, 2014.

[3] R. Wang, *Intelligent microgrid management and EV control under uncertainties in smart grid*. Springer, 2018.

[4] M. H. Rashid, *Power electronics handbook*. Butterworth-heinemann, 2017.

[5] M. Liserre, R. Cardenas, M. Molinas, and J. Rodriguez, "Overview of multi-mw wind turbines and wind parks," *IEEE Transactions on Industrial electronics*, vol. 58, no. 4, pp. 1081–1095, 2011.

[6] F. Blaabjerg, R. Teodorescu, M. Liserre, and A. V. Timbus, "Overview of control and grid synchronization for distributed power generation systems," *IEEE Transactions on industrial electronics*, vol. 53, no. 5, pp. 1398–1409, 2006.

[7] D. E. Olivares, A. Mehrizi-Sani, A. H. Etemadi, C. A. Cañizares, R. Iravani, M. Kazerani, A. H. Hajimiragha, O. Gomis-Bellmunt, M. Saeedifard, R. Palma-Behnke, G. A. Jiménez-Estévez, and N. D. Hatziargyriou, "Trends in microgrid control," *IEEE Transactions on Smart Grid*, vol. 5, no. 4, pp. 1905–1919, 2014.

[8] T. Gönen, *Electric Power Distribution Engineering*. CRC Press, 2014.

[9] M. Z. Kamh and R. Iravani, "Unbalanced Model and Power-Flow Analysis of Microgrids and Active Distribution Systems," *IEEE Trans. Power Del.*, vol. 25, no. 4, pp. 2851–2858, Oct 2010.

[10] V. Yaramasu, M. Rivera, B. Wu, and J. Rodriguez, "Model Predictive Current Control of Two-Level Four-Leg Inverters – Part I: Concept, Algorithm, and Simulation Analysis," *IEEE Transactions on Power Electronics*, vol. 28, no. 7, pp. 3459–3468, July 2013.

[11] A. Mora, R. Cárdenas, M. Urrutia, M. Espinoza, and M. Díaz, "A Vector Control Strategy to Eliminate Active Power Oscillations in Four-Leg Grid-Connected Converters Under Unbalanced Voltages," *IEEE Journal of Emerging and Selected Topics in Power Electronics*, vol. 8, no. 2, pp. 1728–1738, 2020.

[12] P. Acuña, L. Morán, M. Rivera, J. Dixon, and J. Rodriguez, "Improved Active Power Filter Performance for Renewable Power Generation Systems," *IEEE Transactions on Power Electronics*, vol. 29, no. 2, pp. 687–694, Feb 2014.

[13] K. Antoniewicz, M. Jasinski, M. P. Kazmierkowski, and M. Malinowski, "Model Predictive Control for Three-Level Four-Leg Flying Capacitor Converter Operating as Shunt Active Power Filter," *IEEE Transactions on Industrial Electronics*, vol. 63, no. 8, pp. 5255–5262, 2016.

[14] S. Jiao, K. R. Ramachandran Potti, K. Rajashekara, and S. K. Pramanick, "A Novel DROGI-Based Detection Scheme for Power Quality Improvement Using Four-Leg Converter Under Unbalanced Loads," *IEEE Transactions on Industry Applications*, vol. 56, no. 1, pp. 815–825, 2020.

[15] A. S. Vijay, S. Doolla, and M. C. Chandorkar, "Unbalance mitigation strategies in microgrids," *IET Power Electronics*, vol. 13, no. 9, pp. 1687–1710, 2020.

[16] M. A. Hossain, H. R. Pota, W. Issa, and M. J. Hossain, "Overview of AC Microgrid Controls with Inverter-Interfaced Generations," *Energies*, vol. 10, no. 9, 2017.

[17] D. E. Quevedo, R. P. Aguilera, and T. Geyer, *Predictive control in power electronics and drives: basic concepts, theory, and methods.* Springer, 2014.

[18] J. Rodriguez, C. Garcia, A. Mora, S. A. Davari, J. Rodas, D. F. Valencia, M. Elmorshedy, F. Wang, K. Zuo, L. Tarisciotti, F. Flores-Bahamonde, W. Xu, Z. Zhang, Y. Zhang, M. Norambuena, A. Emadi, T. Geyer, R. Kennel, T. Dragicevic, D. A. Khaburi, Z. Zhang, M. Abdelrahem, and N. Mijatovic, "Latest Advances of Model Predictive Control in Electrical Drives – Part II: Applications and Benchmarking With Classical Control Methods," *IEEE Transactions on Power Electronics*, vol. 37, no. 5, pp. 5047–5061, 2022.

[19] P. Cortes, J. Rodriguez, C. Silva, and A. Flores, "Delay Compensation in Model Predictive Current Control of a Three-Phase Inverter," *IEEE Transactions on Industrial Electronics*, vol. 59, no. 2, pp. 1323–1325, 2012.

[20] F. Wang, L. He, and J. Rodriguez, "FPGA-Based Continuous Control Set Model Predictive Current Control for PMSM System Using Multistep Error Tracking Technique," *IEEE Transactions on Power Electronics*, vol. 35, no. 12, pp. 13 455–13 464, 2020.

[21] C. Bordons and C. Montero, "Basic principles of mpc for power converters: Bridging the gap between theory and practice," *IEEE Industrial Electronics Magazine*, vol. 9, no. 3, pp. 31–43, 2015.

[22] A. Bemporad, F. Borrelli, M. Morari *et al.*, "Model predictive control based on linear programming˜ the explicit solution," *IEEE transactions on automatic control*, vol. 47, no. 12, pp. 1974–1985, 2002.

[23] R. P. Aguilera, P. Lezana, and D. E. Quevedo, "Finite-Control-Set Model Predictive Control With Improved Steady-State Performance," *IEEE Transactions on Industrial Informatics*, vol. 9, no. 2, pp. 658–667, 2013.

[24] R. P. Aguilera and D. E. Quevedo, "Predictive Control of Power Converters: Designs With Guaranteed Performance," *IEEE Transactions on Industrial Informatics*, vol. 11, no. 1, pp. 53–63, feb 2015.

[25] S. Vazquez, A. Marquez, R. Aguilera, D. Quevedo, J. I. Leon, and L. G. Franquelo, "Predictive optimal switching sequence direct power control for grid-connected power converters," *IEEE Transactions on Industrial Electronics*, vol. 62, no. 4, pp. 2010–2020, 2015.

[26] A. Mora, R. Cardenas-Dobson, R. P. Aguilera, A. Angulo, F. Donoso, and J. Rodriguez, "Computationally Efficient Cascaded Optimal Switching Sequence MPC for Grid-Connected Three-Level NPC Converters," *IEEE Transactions on Power Electronics*, vol. 34, no. 12, pp. 12 464–12 475, Dec 2019.

[27] J. M. Carrasco, L. G. Franquelo, J. T. Bialasiewicz, E. Galván, R. C. PortilloGuisado, M. M. Prats, J. I. León, and N. Moreno-Alfonso, "Power-electronic systems for the grid integration of renewable energy sources: A survey," *IEEE Transactions on industrial electronics*, vol. 53, no. 4, pp. 1002–1016, 2006.

[28] H. Akagi, E. H. Watanabe, and M. Aredes, *Instantaneous Power Theory and Applications to Power Conditioning*. Wiley-IEEE Press, 2017.

[29] H. Akagi, "Trends in active power line conditioners," *IEEE transactions on power electronics*, vol. 9, no. 3, pp. 263–268, 1994.

[30] F. Blaabjerg, *Control of Power Electronic Converters and Systems: Volume 2*. Academic Press, 2018, vol. 2.

[31] B. Singh and J. Solanki, "An implementation of an adaptive control algorithm for a three-phase shunt active filter," *IEEE Transactions on Industrial Electronics*, vol. 56, no. 8, pp. 2811–2820, 2009.

[32] X. Yuan, W. Merk, H. Stemmler, and J. Allmeling, "Stationary-frame generalized integrators for current control of active power filters with zero steady-state error for current harmonics of concern under unbalanced and distorted operating conditions," *IEEE transactions on industry applications*, vol. 38, no. 2, pp. 523–532, 2002.

[33] N. Mohan, T. M. Undeland, and W. P. Robbins, *Power Electronics: Converters, Applications, and Design*. Wiley, 2002. [Online]. Available: http://www.amazon.com/Power-Electronics-Converters-Applications-Design/dp/0471226939%3FSubscriptionId%3D0JYN1NVW651KCA56C102%26tag%3Dtechkie-20%26linkCode%3Dxm2%26camp%3D2025%26creative%3D165953%26creativeASIN%3D0471226939

[34] A. A. Imam, R. Sreerama Kumar, and Y. A. Al-Turki, "Modeling and simulation of a pi controlled shunt active power filter for power quality enhancement based on pq theory," *Electronics*, vol. 9, no. 4, p. 637, 2020.

[35] H. Akagi, E. H. Watanabe, and M. Aredes, *Instantaneous power theory and applications to power conditioning*. John Wiley & Sons, 2017.

[36] O. Vodyakho and C. C. Mi, "Three-level inverter-based shunt active power filter in three-phase three-wire and four-wire systems," *IEEE transactions on power electronics*, vol. 24, no. 5, pp. 1350–1363, 2009.

[37] P. S. Puhan, P. K. Ray, and G. Panda, "Performance improvement of shunt active power filter with combined control technique," in *2017 International Conference on Emerging Trends & Innovation in ICT (ICEI)*. IEEE, 2017, pp. 56–61.

[38] F. Rojas, R. Cardenas, J. Clare, M. Diaz, J. Pereda, and R. Kennel, "A Design Methodology of Multiresonant Controllers for High Performance 400 Hz Ground Power Units," *IEEE Transactions on Industrial Electronics*, vol. 66, no. 8, pp. 6549–6559, 2019.

[39] I. Etxeberria-Otadui, A. L. De Heredia, H. Gaztañaga, S. Bacha, and M. R. Reyero, "A single synchronous frame hybrid (ssfh) multifrequency controller for power active filters," *IEEE Transactions on Industrial Electronics*, vol. 53, no. 5, pp. 1640–1648, 2006.

[40] J. Rodriguez, M. P. Kazmierkowski, J. R. Espinoza, P. Zanchetta, H. Abu-Rub, H. A. Young, and C. A. Rojas, "State of the Art of Finite Control Set Model Predictive Control in Power Electronics," *IEEE Trans. Ind. Informat.*, vol. 9, no. 2, pp. 1003–1016, may 2013.

[41] J. Rodriguez, C. Garcia, A. Mora, F. Flores-Bahamonde, P. Acuna, M. Novak, Y. Zhang, L. Tarisciotti, S. A. Davari, Z. Zhang *et al.*, "Latest advances of model predictive control in electrical drives—part i: Basic concepts and advanced strategies," *IEEE Transactions on Power Electronics*, vol. 37, no. 4, pp. 3927–3942, 2021.

[42] N. Panten, N. Hoffmann, and F. W. Fuchs, "Finite control set model predictive current control for grid-connected voltage-source converters with lcl filters: A study based on different state feedbacks," *IEEE Transactions on Power Electronics*, vol. 31, no. 7, pp. 5189–5200, 2015.

[43] F. Rojas, R. Cárdenas, R. Kennel, J. C. Clare, and M. Díaz, "A Simplified Space-Vector Modulation Algorithm for Four-Leg NPC Converters," *IEEE Transactions on Power Electronics*, vol. 32, no. 11, pp. 8371–8380, 2017.

[44] M. Rivera, V. Yaramasu, A. Llor, J. Rodriguez, B. Wu, and M. Fadel, "Digital Predictive Current Control of a Three-Phase Four-Leg Inverter," *IEEE Transactions on Industrial Electronics*, vol. 60, no. 11, pp. 4903–4912, Nov 2013.

[45] M. Rivera, V. Yaramasu, J. Rodriguez, and B. Wu, "Model Predictive Current Control of Two-Level Four-Leg Inverters – Part II: Experimental Implementation and Validation," *IEEE Transactions on Power Electronics*, vol. 28, no. 7, pp. 3469–3478, 2013.

[46] P. Karamanakos and T. Geyer, "Guidelines for the Design of Finite Control Set Model Predictive Controllers," *IEEE Transactions on Power Electronics*, vol. 35, no. 7, pp. 7434–7450, 2020.

[47] L. M. A. Caseiro, A. M. S. Mendes, and S. M. A. Cruz, "Dynamically Weighted Optimal Switching Vector Model Predictive Control of Power Converters," *IEEE Transactions on Industrial Electronics*, vol. 66, no. 2, pp. 1235–1245, 2019.

[48] B. Wu and M. Narimani, *High-power converters and AC drives*. John Wiley & Sons, 2017.

[49] S. Vazquez, A. Marquez, R. Aguilera, D. Quevedo, J. I. Leon, and L. G. Franquelo, "Predictive Optimal Switching Sequence Direct Power Control for Grid-Connected Power Converters," *IEEE Transactions on Industrial Electronics*, vol. 62, no. 4, pp. 2010–2020, April 2015.

[50] S. A. Larrinaga, M. A. R. Vidal, E. Oyarbide, and J. R. T. Apraiz, "Predictive Control Strategy for DC/AC Converters Based on Direct Power Control," *IEEE Transactions on Industrial Electronics*, vol. 54, no. 3, pp. 1261–1271, June 2007.

[51] S. Vazquez, P. Acuna, R. P. Aguilera, J. Pou, J. I. Leon, and L. G. Franquelo, "DC-Link Voltage Balancing Strategy Based on Optimal Switching Sequences Model Predictive Control for Single-Phase H-NPC Converters," *IEEE Transactions on Industrial Electronics*, pp. 1–1, 2019.

[52] E. Camacho and C. Alba, *Model Predictive Control*, ser. Advanced Textbooks in Control and Signal Processing. Springer London, 2013. [Online]. Available: https://books.google.com.ec/books?id=tXZDAAAAQBAJ

[53] F. Donoso, A. Mora, R. Cardenas, A. Angulo, D. Saez, and M. Rivera, "Finite-Set Model-Predictive Control Strategies for a 3L-NPC Inverter Operating With Fixed Switching Frequency," *IEEE Transactions on Industrial Electronics*, vol. 65, no. 5, pp. 3954–3965, May 2018.

[54] X. Li, Z. Deng, Z. Chen, and Q. Fei, "Analysis and Simplification of Three-Dimensional Space Vector PWM for Three-Phase Four-Leg Inverters," *IEEE Transactions on Industrial Electronics*, vol. 58, no. 2, pp. 450–464, 2011.

[55] D. Simon, *Optimal State Estimation: Kalman, H Infinity, and Nonlinear Approaches*. Wiley, 2006. [Online]. Available: https://books.google.cl/books?id=UiMVoP_7TZkC

[56] J. Rodriguez and P. Cortes, *Predictive Control of Power Converters and Electrical Drives*. Wiley-IEEE Press, 2012.

[57] O. Kukrer, "Discrete-time current control of voltage-fed three-phase pwm inverters," *IEEE Transactions on Power Electronics*, vol. 11, no. 2, pp. 260–269, 1996.